UNIVERSIDADE DA BEIRA INTERIOR
Engenharia

General Conceptual Design Problems of a Parabolic Solar Sail Structure

Filipe Couceiro Potes

Dissertação para obtenção do Grau de Mestre em
Engenharia Aeronáutica
(Ciclo de estudos integrado)

Orientador: Prof. Doutor José Miguel Almeida da Silva
Co-orientador: Prof. Doutor Pedro Vieira Gamboa

Covilhã, Outubro de 2012

Acknowledgments

The realization of this thesis would not have been possible without the invaluable contribution of several people to whom I wish to express my sincere gratitude.

To Dr. José Miguel Silva, my supervisor, for his unfailing and constant attention, support and encouragement which always kept me motivated throughout all the investigation.

To Dr. Pedro Gamboa, my co-supervisor, for his readiness, suggestions and great dedication that was undoubtedly crucial for the completion of this work.

I am also grateful to Dr. Anna Guerman for her valuable knowledge as well as her important advice during the work period.

Lastly, to Benjamin Schneuwly who played an important role in the early stages of the research, namely during the experimental tests conducted in Chapter 3, for his availability and willingness to help in some of the most difficult phases.

Finally I would like to dedicate this thesis to my relatives and close friends, in particular to my parents and grandparents for their encouragement and for always having believed in me. If it was not for their support, I am sure I would not be where I am today.

Abstract

Solar sails represent a promising and practicable solution for future long-duration space missions involving deep space travel. Since their source of propulsive thrust derives from the energy exerted by solar radiation pressure, they do not depend on any on-board propellant, which thus minimizes energy consumption during a mission and consequently its final costs. However, because in Earth´s vicinity solar pressure presents a very low intensity, and in order to provide the necessary amount of thrust this type of solar-powered spacecraft typically requires an enormous surface area whilst at the same time maintaining the lowest possible mass. Such requirements oblige the adoption of very large structures usually consisting of ultra-thin membranes supported by long slender booms, in the order of tens of meters. This causes some difficulties on the structural design process since the deployment and maneuvering capabilities have to be optimized without compromising the mechanical performance of the whole solar vehicle.

Among the various types of solar sail structural configurations, there is a very ambitious concept considered to be highly efficient, which consists on the parabolic solar sail. In this type of solar-propelled spacecraft, a small mirror designated as the director reflects the sunlight collected from a larger parabolic structure which in turn remains constantly oriented towards the incoming direction of the sunbeams so as to always guarantee the maximum available thrust. Since in this case maneuverability is achieved exclusively by tilting the director component, this allows the entire structure to operate without having to change its inclination in relation to the Sun.

The scope of this work is to explore different possibilities for the conceptual design of a parabolic space structure intended to act as a solar sail collector, with special emphasis on the parabolic shape maintenance issue, since this is crucial for the maximization of the sunlight concentration into its focal point, as well as on its overall structural behavior. On a first approach, a structure which consists solely of an initially flat circular membrane simply supported around its perimeter and without any type of load supporting elements along its radials is considered. In this case, the possibility for the structure to make use of the solar pressure itself as a form of obtaining the desired parabolic curvature is investigated. Assuming the membrane as a perfectly reflecting surface, a parametric study is conducted in order to determine several parameters of interest, as a function of its radius size and thickness. Although the resulting deformed shapes prove to be very similar to parabolic ones, since the obtained focal distances are considerably high, this structural concept does not become feasible for solar sail applications. Consequently, a parabolic boom-based type of structural configuration resembling an open umbrella is considered afterwards. Here, the booms are responsible for guaranteeing the membrane´s parabolic curvature therefore

enabling the focal distance to be initially established during the design phase of the structure. In order to assess its behavior due to solar pressure action, a parametric study is performed to investigate the effects of several design features such as the collector radius, membrane thickness, number of booms, number of supporting points of the membrane along the booms, as well as the effect of a possible angular velocity around the structure´s symmetry axis, with regard to the impact that these have on the resulting loadings and maximum deformations of the entire structure. In the end, the structure´s natural frequencies and mode shapes are also determined.

The obtained results are of upmost importance to the design of an optimized structure which provides greater efficiency in terms of control thrust of the vehicle, thus forming the basis for further more detailed structural and orbital control analysis of this solar propelled parabolic sail spacecraft.

Keywords: Solar sail; Space structures; Parabolic collector; Solar pressure; Circular membrane; Focal distance; Light spot

Resumo

As velas solares representam uma solução promissora e viável para as futuras missões espaciais de longa duração envolvendo viagens no espaço profundo. Uma vez que a sua fonte de impulsão propulsiva advém da energia exercida pela pressão da radiação solar, estas não dependem de nenhum propelente a bordo, o que minimiza assim o consumo energético durante uma missão e consequentemente os seus custos finais. No entanto, devido à pressão solar apresentar uma intensidade muito baixa na vizinhança da Terra, e de modo a fornecer a quantidade necessária de impulso, este tipo de veículo espacial tipicamente requer uma enorme área de superficie, mantendo ao mesmo tempo a massa no valor mais baixo possível. Tais requisitos obrigam à adoção de estruturas de enormes dimensões normalmente constituidas por membranas ultra-finas suportadas por longos *booms*, na ordem das dezenas de metros. Isto causa algumas dificuldades no processo do design estrutural, uma vez que a implantação e capacidades de manobra têm de ser otimizadas sem comprometer o desempenho mecânico de todo o veículo solar.

Entre os vários tipos de configurações estruturais de velas solares, existe um conceito muito ambicioso considerado altamente eficiente, que consiste na vela solar parabólica. Neste tipo de veiculo espacial propulsionado pelo sol, um pequeno espelho designado como diretor reflete a luz solar coletada a partir de uma estrutura parabólica maior que por sua vez, permance constantemente orientanda na direção dos raios solares incidentes de modo a garantir sempre o máximo impulso disponível. Uma vez que neste caso a capacidade de manobra é obtida exclusivamente pela inclinação do componente do diretor, tal permite que toda a estrutura opere sem ter de alterar a sua inclinação em relação ao Sol.

O âmbito deste trabalho consiste em explorar diferentes possibilidades para o projeto conceitual de uma estrutura espacial parabólica destinada a atuar como um coletor de uma vela solar, com especial ênfase na questão da manutenção de uma forma parabólica, uma vez que esta é crucial para a maximização da concentração da luz solar no seu ponto focal, bem como o seu comportamento estrutural global. Numa primeira abordagem, uma estrutura que consiste unicamente numa membrana circular inicialmente plana, simplesmente suportada em torno do seu perimetro, e sem qualquer tipo de elementos de suporte de carga ao longo das suas radiais, é considerada. Neste caso, a possibilidade da estrutura fazer uso próprio da pressão solar como forma de obter a curvatura parabólica desejada é investigada. Assumindo a membrana como uma superficie perfeitamente refletora, procede-se à realização de um estudo paramétrico de modo a determinar diversos parâmetros de interesse, em função do seu tamanho do raio e espessura. Apesar das deformações resultantes provarem ser muito similares a formas parabólicas, uma vez que as distâncias focais obtidas são consideravelmente elevadas, este conceito estrutural não se torna viável para aplicações em

velas solares. Consequentemente, um tipo de configuração estrutural parabólica baseada em *booms* semelhante a um guarda-chuva aberto é considerada numa etapa posterior do trabalho. Aqui, os *booms* são responsáveis por garantir a curvatura parabólica da membrana permitindo assim que a distância focal seja inicialmente estabelecida durante a fase de concepção da estrutura. A fim de avaliar o seu comportamento devido à acção da pressão solar, um estudo paramétrico é efetuado com o intuito de investigar os efeitos de várias caracteristicas de projeto, tais como o raio do colector, espessura das membranas, número de *booms,* número de apoios entre as membranas e os *booms,* assim como o efeito de uma possivel velocidade angular em torno do eixo de simetria da estrutura, no que respeita ao impacto que estes têm sobre as cargas resultantes e deformações máximas de toda a estrutura. No final, as frequências naturais e modos de vibração da estrutura são também determinados.

Os resultados obtidos são de extrema importância para a concepção de uma estrutura otimizada que proporcione grande eficiência em termos de controlo de impulso do veículo, formando assim a base para análises estruturais e de controlo orbital mais pormenorizadas deste veiculo solar parabólico propulsionado pelo Sol.

Palavras-chave: Vela solar; Estruturas espaciais; Coletor parabólico; Pressão solar; Membrana circular; Distância focal; Mancha de luz

Contents

List of Figures

List of Tables

Nomenclature

E	Energy of a moving body or Material´s Young modulus
m_0	Body´s rest mass
c	Speed of light
p	Photon´s momentum magnitude
h	Planck´s constant
v	Photon´s frequency or Material´s Poisson ratio
W_T	Energy flux across a surface
W_E	Energy flux measured at Earth´s distance from the Sun
R_E	Sun-Earth distance
r	Radial coordinate
L_S	Solar luminosity
ΔE	Energy transported across a surface
A	Area of given element surface
Δ_t	Period of time
Δ_p	Momentum exchange across a surface
P	Pressure exerted on a surface
F_i	Force due to incident radiation
α	Surface attitude angle
n_i	Incident radiation direction
F_r	Force due to reflected radiation
n_r	Reflected radiation direction
n	Vector normal to surface element
F	Force exerted on idealized solar sail surface
Ψ_0	Characteristic value of solar pressure in the vicinity of the Earth
w	Transverse displacement
w_0	Maximum transverse displacement
R	Radius of circular membrane

u	Radial displacement at radius
C_1	First integration constant
C_2	Second integration constant
ε_r	Radial strain
ε_t	Transverse strain
U	Strain energy of membrane
W	Work done
Π	Potential energy of an elastic body
t	Thickness of membrane
w_f	Parabolic function
f	Focal distance
θ	Slope of the function at nodes
w_{fi}	Minimized radius spot size
M	Mean percentage error
Y_r	Real deformed coordinate
Y_p	Parabolic deformed coordinate
l	Light spot radius

Chapter 1 – Introduction

1.1 Motivation

Solar sails consist of spacecraft that use the energy supplied by solar radiation as a direct means of locomotion through space in the same way a sailing ship uses winds in our planet (Figure 1). This is effectively possible, since sunlight is composed of a quantity of energy known as photons that act like atomic particles. When these quantum packets of energy are intercepted by the solar sail surface, they impart their momentum to the sail film through two distinct processes, firstly by the initial incidence, and again by reflecting back from it. The force caused by the momentum exchange which results from the combination of both processes is therefore responsible for generating an impulse on the entire structure [1].

Figure 1 - Solar Sail propeled by solar radiation the same way wind pushes a sailing ship [1].

This unique and elegant form of propulsion is significantly advantageous, since contrary to conventional propulsive systems such as rocket engines driven by chemical reactions, solar sails are not limited by an exhaustible energy source, which offers then the added benefit of new mission opportunities at the same time with a much lower monetary cost. Furthermore, as sunlight is permanent, solar sails are also submitted to a constant acceleration limited only by the lifetime of the sail materials in the space environment. Even though this acceleration may be very little at first, this will enable them in a relatively short time to reach very high speeds, far greater than some of those verified with conventional rocket launched craft.

Since at the Earth´s distance from the Sun, i.e. 1 A.U., the momentum carried by the photons is extremely small, solar sails must present a very large surface area while at the same time maintaining the lowest mass as possible. Only so, it is possible to generate a relatively high acceleration from the momentum transported by the largest number of intercepted photons.

Consequently, the structure of this type of spacecraft is generally composed of very large membranes, consisting of highly reflective ultra-thin films such as of Kapton® or Mylar®, which are held in tension by the application of a force field on its edges. These forces can be generated either mechanically from some sort of support structure, namely by long slender booms, or by centrifugal forces induced by the spinning motion of the whole solar sail structure [2].

There are three types of solar sails structural configurations most commonly under discussion namely the three-axis stabilised (flat square sail), the spin-stabilised heliogyro sail and the spin-stabilised disc sail. Nevertheless, despite the great set of advantages that these may present, there is also another very promising solution capable of offering potentially superior performance in terms of acceleration and controllability which is to adopt a parabolic solar sail, also commonly referred to as the compound spacecraft. Although the concept may appear to be relatively recent, it is believed that its preliminary ideas were first discussed in Soviet literature some time ago, namely by Tsander back in the 1970s. More recently, it was studied and subsequently re-invented by some other authors, among which the physicist Robert Forward in the 1990s who coined the term "Solar Photon Thrustor" [3].

When it comes to the more conventional approaches regarding solar sail configurations, one should note that the photons are collected and reflected by the same sheet of material, i.e. the light collector and reflector represent the same structure. As a result, if the desired thrust direction is not directly away from the sun then the sail has to be tilted at some angle with respect to the incoming sunlight direction. This results in a loss of propulsive efficiency of the sail, since as it is tilted the effective photon collecting area is reduced. However, as in a parabolic solar sail the functions of collecting and directing the solar radiation are separated, this trend will not be verified.

Generally speaking, the parabolic solar sail is composed of a large reflecting surface (similar in size and mass to that of a conventional solar sail) known as the collector that directs the incoming solar radiation into a system of much smaller reflecting mirrors which in turn can be subdivided in two different arrangements [4] according to the number of mirrors: consisting solely by a director - the SSPT (Single Solar Photon Thrustor) shown in Figure 2, or by of a reflector and a director - the DR SPT (Double Reflector Solar Photon Thrustor) presented in Figure 3. In either case, the collector is designed to be always in a sun-facing attitude so as to ensure the maximum area of sunlight exposure, which means that this type of solar sail configuration will always have a superior performance in terms of maximum propulsive thrust. The director, which consists of a small flat mirror that can be tilted at a determined angle, reflects the incoming light rays coming from the collector on a specific desired orientation, hence, the responsibility of defining the thrust vector and consequently controlling the motion of the spacecraft, is attributed to this component. However, in order to accurately

focus all the incoming sunlight into the director (or reflector depending on the type of arrangement considered) it becomes understandable that the collector necessarily has to present a parabolic surface. Only then, it is possible to concentrate the sunlight onto a specific point of the space environment designated by the focal point, which should coincide with the director´s (reflector´s) position. It is evident that the accurate maintenance of the collector´s parabolic geometric shape becomes therefore an issue of paramount importance, since it is mandatory for the maximization of the available thrust of the whole spacecraft. Despite the fact that the parabolic solar sail may present a significant mass penalty in contrast to the standard flat solar sail configurations, it has the added benefit of providing a potentially superior performance in terms of maximum propulsive thrust, a less complex control system (the entire spacecraft does not need to be rotated thus not compromising as much its structural integrity) as well as a maximum capacity for useful load. All these advantages make this solar sail concept particularly attractive.

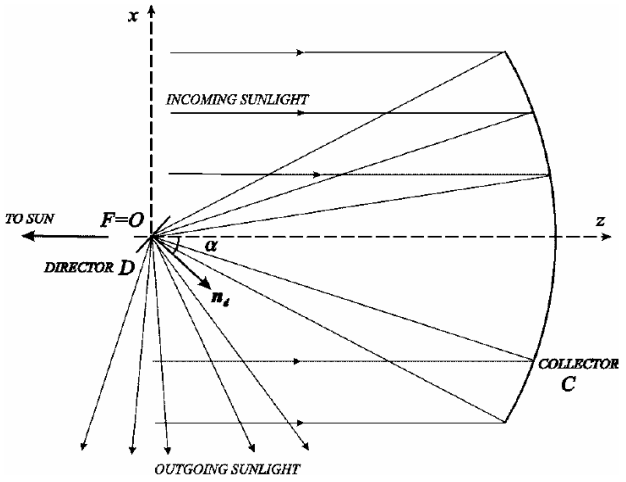

Figure 2 - SSPT structural configuration [4].

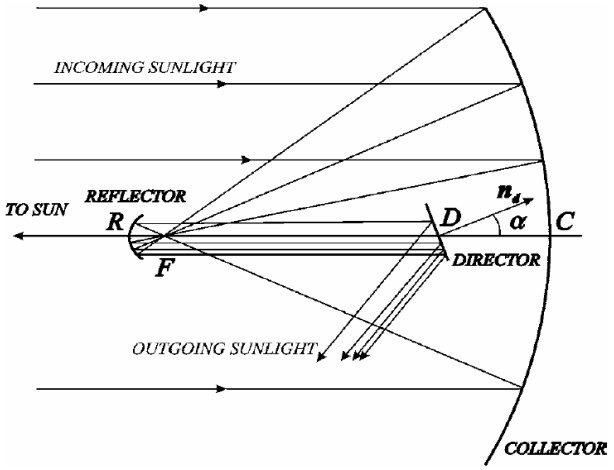

Figure 3 - DR SPT structural configuration [4].

1.2 Objectives

The present thesis is subdivided in three main distinct parts, all of which are essentially based on a set of numerical simulations carried out using the finite element code ABAQUS® v6.11-3.

In the first section, some initial studies are performed in order to gain further insight into the proper modelling of membrane elements by resorting to the finite element method. The goal is to understand how the maximum deformations of the membranes vary according to different material properties, section definition types as well as boundary conditions. Additionally, experimental measurement tests are also conducted in the chapter´s last part, so as to validate some of the results obtained during the numerical simulations.

The second part aims at assessing the feasibility of creating a parabolic solar sail collector, whose structural concept is characterized only by an initially flat circular membrane translationally constrained around its perimeter and without any type of load supporting elements along its radials. In particular, it is intended to explore and to validate the hypothesis of the membrane in making use of solar pressure as a means of obtaining the required parabolic curvature, once this would greatly simplify and lighten the structure of the spacecraft, therefore having considerable advantages when compared for example to a boom--based type of structural configuration. With this objective in mind, a parametric study is performed to determine some crucial parameters of interest, namely the resulting approximate focal distances together with the respective light spot diameters on the focal plane, taking into consideration the variation of both the radius size and thickness of the membrane. In order to do so, the nodal displacement profiles along the membrane´s radials need to be first computed for each case. During the analyses, an analytical method capable of determining the mid-point maximum displacements together with the focal distance for a perfect parabolic surface is also presented as an additional tool for results correlation.

Differently to the previous studies which are mainly focused on the behaviour of membrane based structural parts in space environment, the last part takes in consideration the adoption of a parabolic collector design constituted by several booms and membrane gores as well as a small mast in the middle, thus resembling an open umbrella type of structural configuration. In this case, since the parabolic shape is ensured by the curvature provided by the stiffness of the booms, the structure´s focal distance may be featured as an initially known variable, once this is defined during the design phase. The objective of this study consists on evaluating the influence of several design parameters with regard to the impact that these have on the resulting loadings and maximum deformations of the entire structure when under the effect of solar pressure. These include varying the collector radius size, membrane thickness, number of booms, number of supporting points of the membrane along the booms, as well as to take into consideration the effect of a possible angular velocity around the structure´s

symmetry axis. A different geometrical concept for the membrane gores is also addressed. Ultimately, the collector´s natural frequencies and the respective mode shapes are also extracted in order to characterize its dynamic response.

1.3 Literature review

1.3.1 Historical perspective

Although only relatively recently solar sails have reaffirmed themselves as an innovative and practical mean of spacecraft propulsion, its concept has already a long and vast history, dating back to the Soviet pioneers, and probably even before that.

It all first started back in 1873 when the Scottish physicist James Maxwell predicted the existence of radiation pressure as a consequence of his unified theory of electromagnetic radiation [5]. The first experimental results of his theory were then demonstrated by the Russian physicist Peter Lebedew in 1900 at the University of Moscow. Between this period some French authors, notably Faure and Graffigny wrote about spaceships propelled by mirrors, however, it was not until the beginning of the 20th century that the concept of a solar sail was more accurately established as an engineering principle. The credit of such principle is attributed to the Latvian engineer Fridrickh Tsander considered the first to write about solar sailing practicability in 1924. It is thought though, that his ideas had been in part inspired by Tsiolkovsky, considered the Soviet father of astronautics, who had already written before in 1920 about the potential use of space propulsion using light.

Following the initial development work by Tsander and Tsiolkovsky, the concept of solar sail took approximately thirty years to be re-invented and published in literature. It was only in 1951 that the American aeronautical engineer Car Wiley explored the fundamental benefits of solar sails for a range of mission applications comparatively to chemical propulsion systems. Subsequently in 1958, Richard Garwin authored the first solar sail paper in the Journal *Jet Propulsion* where he coined the term "solar sailing". He recognized, for instance, the potential advantages of solar sails to reach very high velocities over a relatively short period, since these would be continuously accelerated. After Garwin´s standpoint about solar sailing, several studies regarding solar sails orbits and trajectories, were undertaken during the period between the late 1950s and early 1960s.

Yet, it was not until the early 1970s, which coincided with development of the Space Shuttle, in addition to technological advances with deployable space structures as well as thin films, that a solar sail could probably find a practical application for a specific mission. By 1973 NASA considered the use of solar sails as a potential propulsion system for performing a rendezvous mission with Halley's Comet during its 1986 flyby of earth [6]. However, the required level of solar sail performance for this specific mission suggests that the study might have been considered too optimistic given the immature technology of the time in this area.

1.3.2 Technological developments

Following Halley's Comet first studies with solar sails, it was not until the early 1990s that the concept once again regained its technological interest, although to this day, practical experiences with solar sails are still very limited.

In 1993 the Russians were the first to successfully deploy a spinning solar sail-like structure in space. The sail in question called *Znamya* 2 (Figure 4) consisted of eight pie-shaped panels fabricated from 5 millimetres thick PETF (a Russian version of Mylar®) film with no supporting structure [7]. It was deployed from an unmanned spacecraft after it had initially completed its first mission of sending supplies to the Mir space station. Then, after being undocked from the Mir, due to the spinning induced form the spacecraft vehicle containing the sail structure, using the resultant centrifugal acceleration a circular 20 meter diameter sail/reflector was finally unfolded. Although its intended purpose was to demonstrate the capability of space based mirror technologies in providing sunlight from space to arctic regions in Russia, most of the technologies verified for the *Znamya 2* were directly applicable to the principles of solar sailing [8]. In 1999, the deployment of a second larger 25 meter diameter reflector *Znamya 2.5* failed, due to a mission operations and software error [9].

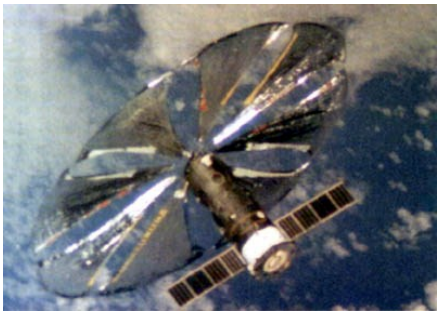

Figure 4 - An artist´s concept of *Znamya* 2 [8].

Figure 5 - DLR´s solar sail prototype [10].

Towards the end of 1999, the first ever ground deployment of a solar sail structure was demonstrated in Cologne by DLR (*Deutschen Zentrum fur Luft-und Raumfahrt*) in collaboration with ESA (European Space Agency). The structure in question was a 20 meter side square solar sail with four deployable booms with a length of 14 meters each (Figure 5). The main objective of this ground-test was to evaluate the storage, but most of all, the deployment capabilities of the booms under simulated zero-g conditions. Due to the significant progress in developing lightweight deployable structures using advanced materials, including carbon fibre reinforced plastics (CFRP´s) which have matured over the past decades these were chosen as the DLR´s solar sail booms materials, since they were able to combine high strength and stiffness with low density at the same time. As it may be seen in Figure 6, the booms consist of two laminated sheets which are bounded at the edges to form a tubular "omega" shape [10]. Therefore, they can be easily pressed flat and stowed around a central

payload volume (the deployment module shown in Figure 7) for storage, and uncoil from it during the deployment sequence. Once deployed, the booms resume their original tubular "omega" shape, serving as the points of attachment to the sail material.

Figure 6 - CFRP deployable boom used by DLR [8].

Figure 7 - DLR´s solar sail deployment module [11].

Each sail segment used in the DLR´s experiment consisted of right isosceles triangles fabricated in Mylar® with a thickness of 12 microns coated with aluminium on one side. However, other film materials were considered for the sail segments including substrates of Kapton® and Teonex® (PEN). The purpose for using different materials was to assess the film´s handling, processing and to evaluate the material´s behaviour for seaming, folding, as well as for sail deployment [11].

Presently, Kapton® and Mylar®, brand trademarks patented by *Dupont* (the company that manufactures these types of polymers), are considered for sure the most suitable materials for solar sail membrane applications due to their extreme low weight and good reflecting properties. Kapton® (Figure 8) presents a good resistance to radiation and it is capable of maintaining its physical and mechanical properties over a wide range of temperatures. Mylar® (Figure 9), on the other hand, may also be considered a good candidate essentially due to its low density, which makes it a slightly lighter material in comparison to Kapton®. However, its main drawback is that it has poor resistance to solar UV radiation, therefore making it unsuitable for very long exposures [2]. For this reason, when it comes to the application in solar sails membranes, this kind of material is typically coated on both its sides.

Figure 8 - Kapton® substrate sample [12].

Figure 9 - Sheet of reflecting Mylar® [13].

Usually, the surface which is orientated towards the incoming solar light is coated with a highly reflective foil, such as aluminium, in order to promote the reflective characteristics of the material. Thus, a higher degree of acceleration is achievable, once the resulting momentum exchange between the surface and photons can be almost doubled. Consequently, as the absorbed light deposits energy in the sail film, the back side surface must be designated to work as a radiator [1]. This way, the material can be held at a constant temperature so that it does not deteriorate. Even though such materials may be considered to have acceptable properties for the time being, the truth is efforts have been made in order to obtain more durable and lightweight materials in the near future.

Another important milestone in the history of solar sails culminated with the project *Cosmos* 1 developed by the U.S based Planetary Society together with Russia. Its purpose was to conduct the first mission of a solar sail flight. Once in orbit, the structure (Figure 10) would have been deployed through the use of inflatable booms forming a set of 8 triangular blades resembling a heliogyro solar sail configuration. Each of the triangular blades, made of aluminized Mylar® with 5 micron of thickness, would have the ability to be rotated in order to alter the direction of the thrust vector, therefore allowing the entire structure to be controlled in orbit. However, the Russian rocket carrying it, a converted submarine-launched ballistic missile, failed to separate from the third stage of the rocket, and as a result the sails and the re-entry capsule failed to deploy. If it had been successful, it would have probably been the first solar sail to actually fly in space.

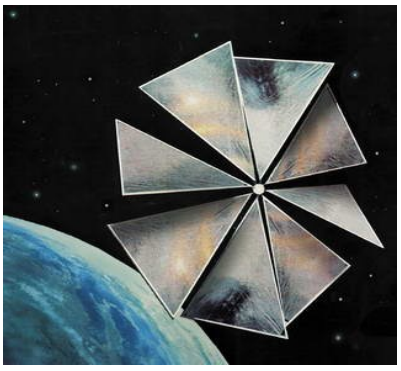

Figure 10 - Sketch of the *Cosmos* 1 [8].

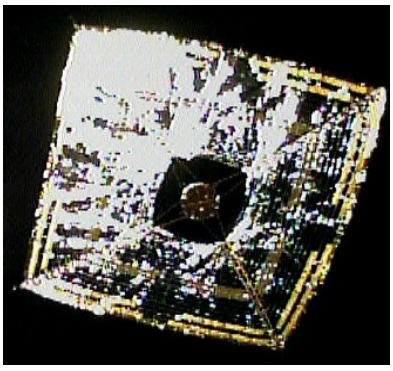

Figure 11 - Solar Sail IKAROS [15].

Despite all the growing research over the last years on this topic, the merit for the world´s first actual solar sail to successfully deploy on an interplanetary orbit goes to the Japanese. The solar sail in question (Figure 11) called "IKAROS" (Interplanetary Kite-craft Accelerated by Radiation of the Sun), was developed by JAXA (Japan Aerospace Exploration Agency), and was launched on May 21st, 2010 onboard an H-IIA launch vehicle as a payload alongside the Japanese Venus Climate Orbiter, AKATSUKI. IKAROS is equipped with a 20 meter diagonal length square membrane made of a polyimide film with a thickness of approximately 7.5 micrometers. The membranes consist of four trapezoid petals with thin solar cells and

steering devices [14], each of which is connected by bridge-elements made of a hook-and-loop fastener (Figure 12). The solar cells have a thickness of 25 micrometers and are made of amorphous silicon. These allow for electricity generation in addition to the acceleration gained by the solar radiation. Consequently, due to the electrical power generated, steering devices consisting of liquid crystals can be switched with variable reflectance thus allowing attitude control. The petals of the membrane are connected to the main body, which has a diameter of 1.6 meters, mechanically and electrically by tethers and harnesses, respectively. These, in turn can be accordion-folded forming long strips which form a cross-shape after being connected together. This method is considered to be relatively simple and suitable to create and stow thin large membranes [15].

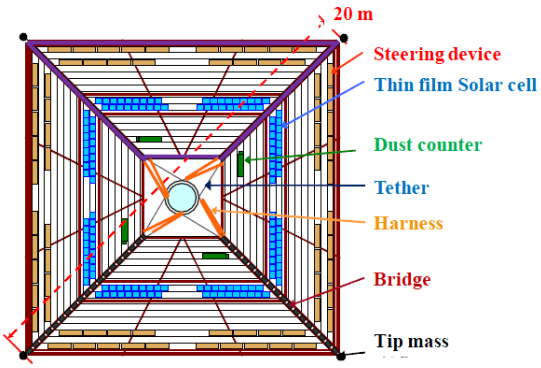

Figure 12 - IKAROS configuration [16].

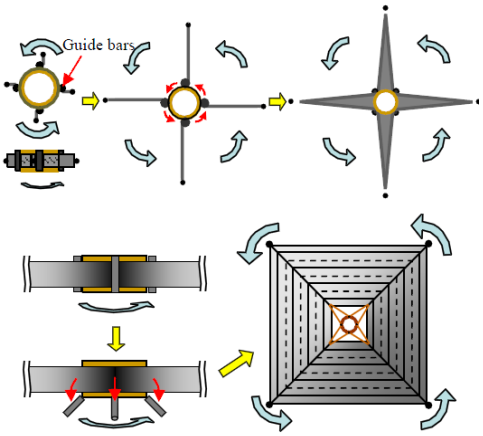

Figure 13 - IKAROS deployment stages [15].

The uniqueness of the solar sail system adopted for IKAROS is that, even though this may be distinguished as a square type solar sail, it is deployed and kept extended only by using the resulting centrifugal force due to the spacecraft's spinning motion. Thus, it does not need any sort of support structure to keep the structural shape of the sail, which contributes to a simple and lightweight sail system [16]. Regarding the deployment sequence of the membranes this can be divided in two stages. In the first one (Figure 13 upside) the strips are quasistatically reeled out by rotating four guide bars along the surface of the sail. Notice that at the end of each tether, a 0.5 kilogram mass is attached to easily guarantee and support the deployment and the extension of the sail by the centrifugal force due to the spinning motion. At the end of this stage, the sail is therefore extended forming the above-mentioned cross-shape. In the second stage of deployment process (Figure 13 downside) the strips are dynamically unfurled, i.e. the guide bars are unlatched and the petals deployed dynamically.

Despite the efficiency of the stowing and deployment procedures verified in IKAROS, one should note that these processes still keep representing a major challenge in the design of a solar sail structure. Such procedures may seriously compromise the consistency of the membrane´s materials as well as the integrity of the whole structure, being probably the reason why so many solar sail missions were unsuccessful over the last years.

1.3.3 Researches based on finite element analysis

Regardless of the type of configuration adopted, very large structures such as the ones of solar sails, usually consisting of very long slender booms with ultra-thin membranes, inevitably become very elastic and therefore susceptible to deformations and low frequency vibrations which may affect the propulsion performance and the effective control of the overall vehicle. Consequently, these types of structures may get very difficult to design and analyse, not only because of their enormous dimensions, but also due to the possible nonlinear structural behaviour that may arise. In addition to these difficulties, mainly due to the effects of gravity and the presence of air in our planet, it is practically impossible to perform full scale structural response measurements on solar sails with an accurate representation of the space environment via ground laboratory tests. Indeed, even the world´s biggest thermal vacuum chamber is not big enough to handle such large structures. Therefore, in order to assess and predict a solar sail´s structural behaviour, it is often necessary to rely on high fidelity computational methods capable of conducting virtual tests. One way to predict such structural and dynamic behaviour is by using the finite element method. Currently there are a set of well-known structural analysis packages, such as for instance ABAQUS®, NASTRAN® and ANSYS®, which resort to the finite element method for this purpose. Several solar sail computational studies using this numerical technique for structural analysis purposes have been published by some authors.

Sleight and Muheim [17] performed parametric studies using ABAQUS® on two generic square solar sail design concepts in order to investigate parameters of interest, namely the effects of sail size, sail membrane thickness and sail pre-stress on the sail frequencies and deflections together with the effects of boom thickness on the sail membrane and boom deformations, vibration frequencies, etc. Both concepts had four 106 meter booms made of composite material, four triangular membranes made of Kapton® as well as a 2 meter control mast. However, on one concept the membranes were attached to the booms by cables at five distinct points whilst on the other with multiple points along the length of the booms (Figure 14). By submitting the cables to a fictitious thermal load, this allowed to simulate the membranes pre-tension as a consequence of the resultant contraction induced by the cables.

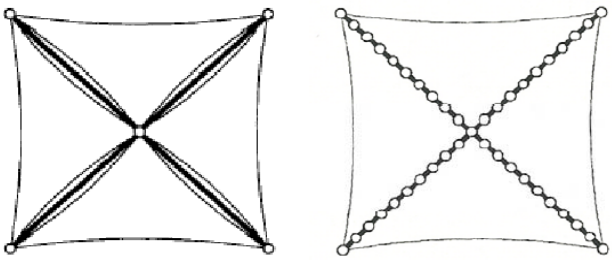

Figure 14 - Two square solar sail design concepts used in reference [17].

All analyses included geometric nonlinearity and the use of the inertia relief feature, since this allows balancing externally applied loads on a free flying sail, i.e. an unconstrained structure, with inertial loads developed due to its acceleration. The main purpose of this investigation was to use the parametric studies results as a means of identifying the general response trends associated with key parameters in the design of solar sails, and areas of potential nonlinear structural interactions for future studies.

A study carried out by a team in the University of Science and Technology of China [18] performed structural analyses using the finite element method also on a square type solar sail with the software ANSYS®. The sail consisted of four right-angled triangular Kapton® films deployed along four CFRP booms each made up of five segments. An interesting feature of this work was that besides the loads of solar pressure, the effects of temperature on the sail were also considered. After some assumptions had been taken for the model, in order to simplify the computation, the deflections (Figure 15) and stress distribution on the sails were obtained. It was verified that after applying two states of loads during the analysis, one applying the solar radiation pressure only and the other both solar radiation pressure and temperature, the effects of temperature had almost no impact on the deflection of the sail, so the deflection depended almost entirely on the effects of solar pressure.

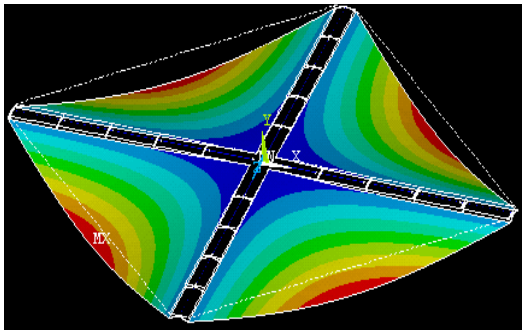

Figure 15 - Deflections after solar pressure and thermal load have been applied [18].

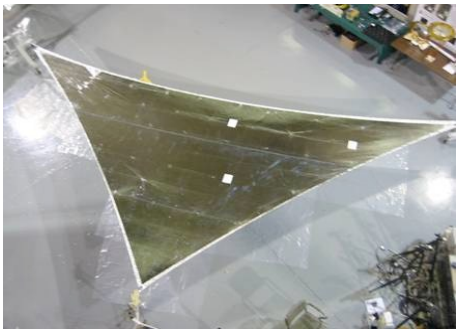

Figure 16 - Static test on solar sail membrane experimental model [19].

Some other researches have been conducted bearing in mind not only the results obtained by numerical methods, but more importantly to correlate them with the ones obtained from experimental testing. A work described in a paper which was funded by the In-Space Propulsion Technology Program [19] considered a single quadrant of a 10 meter square solar sail structure consisting of a central hub, two self-supporting booms, and a triangular membrane made of aluminized CP1 material. It was successfully modelled, using finite element analysis with MSC/NASTRAN® and later also with ANSYS® as a comparison of parallel analyses. Consequently, static deflections and ground vibration tests were also performed at ambient atmospheric conditions (Figure 16). The test results obtained were therefore used to validate the finite element analyses predictions, and in conclusion, they were not very different from each other.

Other studies involving finite element analysis, however, have addressed to more specific aspects regarding solar sail´s structural behaviour. The wrinkling phenomena for instance, which may occur on solar sail´s membranes is a frequently discussed subject. Wrinkles develop since membranes have very low thickness which implies that its bending stiffness is practically negligible, as well as its resistance to compressive loads. Therefore, it is only when the membranes are submitted to some degree of pre-tension, that some level of stiffness will be present. However, unless the distribution of this in-plane tension is absolutely uniform, which in reality is very hard to achieve accurately, the membranes will most certainly wrinkle. In the case of solar sails membranes the formation of wrinkles have to be avoided as much as possible since its presence may detrimentally affect some important parameters, such as its static and dynamic performance as well as its reflectivity. In fact, if wrinkles cover a vast portion of the sail, the lower will be the exerted solar pressure with respect to what would be expected for a flat smooth surface, thus making the sails ability of reflecting light to be reduced. Furthermore, the sail´s material lifetime may also be compromised, as wrinkling may cause the material to locally absorb more energy than it would in normal conditions which may lead this to overheat after a short period of utilization. Some authors have studied the formation of wrinkles and their consequent effects on the structural behaviour of large membranes including the ones of solar sails.

Wong and Pellegrino [20] investigated the wrinkling of an elastic flat square membrane, applicable to a solar sail, subjected to two pairs of equal and opposite concentrated forces (T1 and T2) uniformly distributed at the four corners. They observed two wrinkling regimes by means of finite element analysis, namely with ABAQUS®, in order to accurately estimate wrinkle patterns and average wrinkle amplitudes and wavelengths. In addition, an analytical approach and experimental measurements were also performed. During the finite element simulations, the first wrinkling regime considered a symmetric loading of 5 Newton in each corner. It was observed that a symmetric wrinkling pattern was evident for the membrane, even though the wrinkling amplitudes were very small. In the second wrinkling regime, T2 was maintained at 5 Newton, and T1 was increased up to 20 Newton. In this case however, a large diagonal wrinkle between the two more heavily loaded corners was observed, as well as a number of smaller wrinkles near the corners of smaller loads (Figure 17).

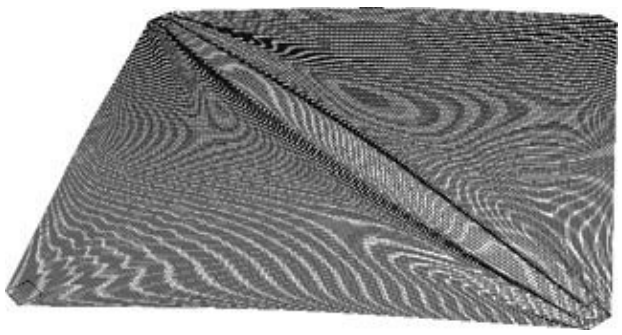

Figure 17 - Wrinkled shape obtained for the two more heavily loaded corners case [20].

In another recent study Tessler and Sleight [21] carried out two numerical studies with the ABAQUS® FEM code in order to gain further insight into the proper modelling of wrinkling deformations states in statically loaded, tensioned thin film membranes exhibiting regions of high stress concentration. The model of study consisted of a flat square membrane made of Kapton® which was uniformly loaded along four truncated edges at its corners with tensile forces acting in opposite directions along the two diagonals. It was demonstrated that excessive mesh refinement in regions of stress concentration would be disadvantageous in achieving wrinkled equilibrium states and that relatively small changes in the size of the truncated region produced distinctly different wrinkling deformations, including their patterns, wavelength and depth.

It should be noted that work in this area has mostly been limited for the square solar sail configuration type. This is probably related to the fact that according to the mission's requirements recently imposed, among the other types of configurations the square sail is probably still seen as the best possible choice for long-term development. This may be related in part due to its less severe dynamic problems, such as vibrations and oscillations, since by definition this configuration is not submitted to spin motion as is the case with the other types, its relative thermal stability, which in turn does not compromise to the same extent the mechanical performance of the sail´s materials, together with its effective manoeuvring capabilities, allowing for instance to provide rapid turning rates which may be required for planetary escape and capture spirals. Putting all these factors together, they all contribute to the simplicity of operation verified on the square sail configuration type.

Even though the parabolic solar sail concept may appear to be very attractive in principle, from what it has been established during the literature research, little efforts have been made regarding engineering studies involving structural analysis methodologies for this specific case of study. Nevertheless, some studies regarding structural analysis of space parabolic structures have been performed, though most of them are related to some other applications, such as in large deployable reflectors used for satellite communication and radio astronomy as well as for instance in solar-powered concentrators. More recently there has also been an increasing attention on the parabolic inflatable membrane structures due to their ability of achieving low weight and prospects of a good shape accuracy. Of course, regardless of their possible applications, such structures are always extremely reliant on the accuracy of its parabolic shape maintenance in order to ensure maximum performance.

Pellegrino [22] proposed the design of a new concept of large deployable membrane reflectors suitable for applications such as satellite communication and Earth observation, known as the *Collapsible Rib-Tensioned Surface* (CRTS) reflector. This consisted of a central expandable hub with a number of thin-walled foldable ribs connected to it, together with a precision shaped membrane supported and tensioned by the ribs (Figure 18). A parabolic

offset (off-axis) configuration was considered for the shape of the reflector, since this is of great interest for communication satellites. This offset configuration derives from the interception of a parent paraboloid with a circular cylinder of diameter *D*, whose axis is parallel to the axis of the paraboloid. In order to investigate the feasibility of the CRTS reflector, the reflector´s shape approximation to a perfect paraboloid was carefully analysed. To do so, the accuracy of this approximation was measured in terms of an overall root mean square error relating to the deviation of the obtained surface from the best fit paraboloid. Two different reflector geometries, an offset configuration (with distance from the focal axis of the parent paraboloid to the near side of the edge of the reflector equal to 1 meter) and a symmetric configuration were considered in this case. Both geometries had an aperture diameter of 10 m and a focal length of 7.8 m. It was verified that the surface errors of the two reflectors depended on the number of ribs, i.e., as long as the number of ribs were increased, the magnitude of the root mean square errors decreased considerably, being that an accuracy of about only approximately 2 mm was achievable, despite a high number of ribs, namely 24, had to be considered for this effect.

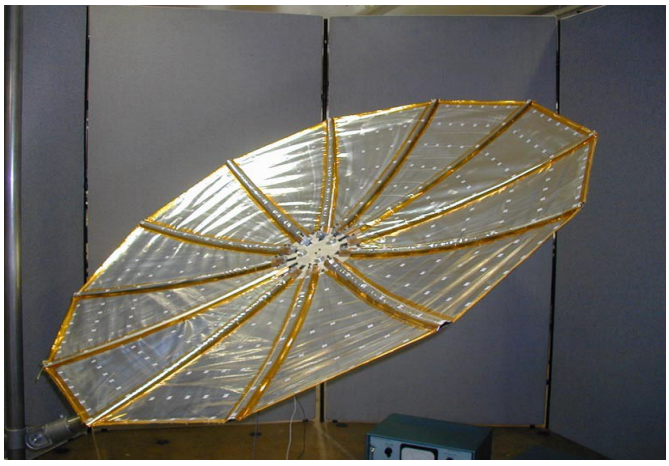

Figure 18 - Prototype of CRTS offset reflector [22].

Marker and Jenkins [23] demonstrated that by imposing appropriate boundary perturbations, namely outward radial displacements along specific positions around a circular boundary of a thin inflatable membrane, the deviation of the obtained surface profile from that of an intended parabolic form could be reduced. In order to do so, finite element analysis were carried out using ABAQUS® and the figure error (the measure of the deviation of the actual surface from that of a desired configuration) was estimated for three different situations on a quarter symmetry model. The first considered the inflation only without any boundary displacements and the second and third considered an outward radial displacement of 2.54 mm for three angular positions (0, 45 and 90 angular degrees along the model boundary) and for two angular positions (0 and 90 angular degrees along the model boundary) respectively. The results were always taken along a 45 degree meridian regardless the considered boundary displacements. It was shown that the three boundary displacements case enabled the

maximum reduction in the figure error, although the two boundary displacements case could already made significant reductions in comparison to the first case (inflation only).

Yan Xu and Fu-ling Guan [24] addressed initial shape analysis, cutting-pattern analysis methods, surface accuracy measurements, modal testing and radio frequency characterizations on a high-precision inflatable membrane reflector model intended for spaceflight applications. A cutting-pattern analysis method was responsible of determining the required cutting patterns as well as the shapes of a given number of gores which were initially cut from a planar membrane for later being assembled to form the model´s three dimensional reflective surface. This cutting-pattern analysis method was based on a spring-mass system that represented a triangular membrane element. In order to validate these analytical methods, a 3.2 meter experimental model was designed, manufactured and assembled for testing (Figure 19). In addition to the reflective surface, the model also consisted of a canopy, a support structure, an adjustment cable system and a series of catenaries around the reflector. Consequently, the surface accuracy of the reflecting surface of the model was analysed using a non-contact measurement approach, namely by a photogrammetric measuring system equipped with *PhotoModeler* software packages. It was demonstrated that after multiple shape adjustments, accomplished by changing the tension in the cables responsible for mounting the reflector to its support structure, the surface shape accuracy defined by its RMS (Root Mean Square) error from a best fit parabolic shape, was less than 1mm. Regarding the dynamic analysis, a simulation was carried out with ANSYS® software, which by resorting to the *Lanczos* method, allowed to determine the first mode frequency of the FEM model, in which the reflector was defined as a shell element and the catenaries and support structures as beam elements. The simulation results demonstrated to agree well with the analytical predictions. In the end, the radio frequency characterization also showed that the radiation pattern of the reflector was well focused.

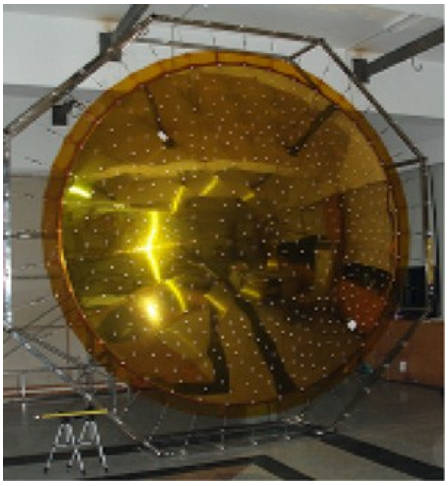

Figure 19 - Experimental model used [24].

Figure 20 – 0.3 meter reflector antenna dish [25].

Sreekantamurthy et al [25] performed structural analysis in order to predict both static and dynamic numerical response characteristics of ultra-thin inflatable parabolic membranes for antenna reflectors. During the research, three distinct parabolic antenna concepts of different sizes and shapes were considered; a 0.3 meter subscale reflector inflatable dish antenna (Figure 20), a 2 meter half-scale hybrid inflatable antenna and a full-scale 4 by 6 meter off-axis parabolic reflector antenna for the analysis. The main objective of the study was not only to use the computational results as future form of validation of the experimental models, but also to explore different analysis techniques for the antennas structural response prediction. These included various aspects such as nonlinear analysis methodologies, iterative solution methods, sensitivity of response to structural loads, namely internal inflation pressure, gravity and pretension loads as well as approaches to membrane wrinkling characteristics. Both NASTRAN® and ABAQUS® commercial codes were used in parallel during the finite element analysis performed on the three models. Figure 21 shows an example of a static implicit analysis performed with ABAQUS® on the 0.3 meter off-axis parabolic reflector membrane finite element model. In this case, it is possible to observe the model´s displacement patterns when under growing catenary tension loads and also subjected to 1G gravity load. The obtained maximum displacement results were a little lower than those verified during the NASTRAN® analysis, since a higher modulus for the catenaries needed to be specified in order for the solutions to converge. According to all the simulations performed during the research, it was found that the antenna reflector surface accuracies were very much dependent on its size and shape as well as for instance on the spacing between the catenaries and the amount of applied loads.

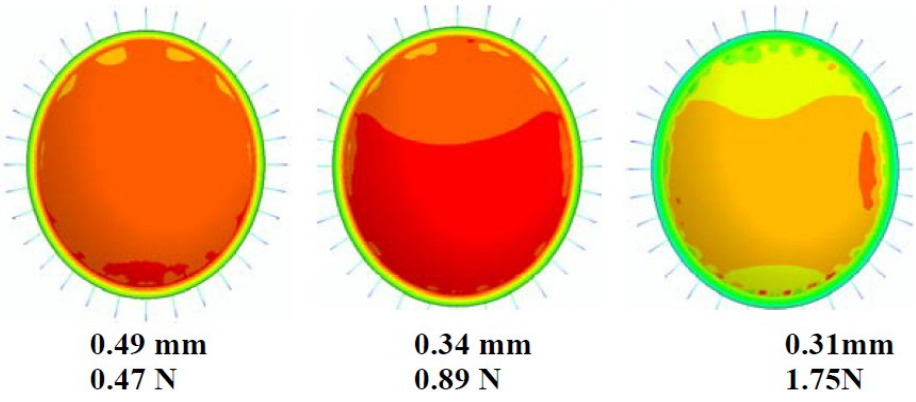

Figure 21 - Displacement patterns for 0.3m numerical model [25].

Chapter 2 – Theoretical background

2.1 Solar radiation pressure physics

The quantum mechanics theory allows giving a good description of the physics behind the existence of the solar radiation pressure as being a result of the momentum transfer process between the solar photons and a given surface [2]. This is true since the momentum transported by the photons is a conservative quantity, i.e., the principle of conservation of momentum becomes valid for this situation. Therefore, this process is ultimately responsible for allowing such vehicles to gain acceleration in the space environment.

According to the special theory of relativity proposed by Albert Einstein which describes the physics of motion in the absence of gravitational fields, an expression capable of providing the total energy E of a moving body may be given by

$$E^2 = m_0^2 c^4 + p^2 c^2 \tag{2.1.1}$$

where m_0 is the rest mass of a body, p its momentum and c is the speed of light. Since photons have zero rest mass, the energy due to its motion may be rewritten in the following form:

$$E = pc \tag{2.1.2}$$

On the other hand, the Planck´s law states that each energy element is proportional to its frequency v which is given by the famous equation

$$E = hv \tag{2.1.3}$$

in which h is the Planck´s constant. Therefore, by combining the photon energy defined in the two previous equations, i.e., special relativity with quantum mechanics, the momentum transported by a single photon may be written as

$$p = \frac{hv}{c} \tag{2.1.4}$$

In order to determine the pressure exerted on a given body, the momentum carried by a flux of photons has to be considered. In this regard, the energy flux W_T, which consists of the energy per unit area in unit time, is given by

$$W_T = W_E \left(\frac{R_E}{r}\right)^2 \tag{2.1.5}$$

Consequently, at the Earth´s distance from the Sun, the energy flux W_E in terms of the solar luminosity L_S takes the form:

$$W_E = \frac{L_S}{4\pi R_E^2} \tag{2.1.6}$$

Concerning the energy flux definition, it is also know that the energy ΔE transported across a surface of a given area A normal to the incident radiation in a given period of time Δt may be written as

$$\Delta E = W_T A \Delta t \tag{2.1.7}$$

Consequently, as this energy transports momentum Δ_p, based on equation (2.1.2) this results that

$$\Delta_p = \frac{\Delta E}{c} \tag{2.1.8}$$

Next, according to *Newton´s* second law of motion, in terms of pressure P exerted on a given surface, this can be defined as the momentum transported per unit time per unit area so that

$$P = \frac{1}{A}\left(\frac{\Delta p}{\Delta t}\right) \tag{2.1.9}$$

Finally, by replacing equations (2.1.7) and (2.1.8) into the previous formula, the pressure exerted on a given surface due to photon moment transfer is therefore given by

$$P = \frac{W_T}{c} \tag{2.1.10}$$

The energy flux across a surface measured at the Earth´s distance from the Sun features a mean value of approximately 1368 J $s^{-1}m^{-2}$. Therefore, and since the speed of light matches 3.0E^8 m s^{-1}, according to the last equation, the solar pressure characteristic value in the vicinity of Earth Ψ_0 is taken to be 4.56E^{-6} N m^{-2}. However, when considering and idealized surface, i.e., a perfectly reflecting surface film, the observed solar pressure takes a value of 9.12E^{-6} N m^{-2} which is twice the value provided by equation (2.1.10). This is true since for this situation the momentum transferred to the surface due to the reaction caused by reflected photons is in theory identical to the momentum transferred to the surface by the incident photons, thus making the resulting momentum exchange between the photons and the surface to be doubled. It should also be noted that the energy flux, and therefore the solar radiation pressure magnitude, decreases as the distance to the Sun becomes greater. Consequently, for a given solar sail surface, as this finds itself further away from the Sun the lower will be the acceleration to which it will be subjected.

2.2 Forces on a perfectly reflecting solar sail

In this section, the forces exerted on an ideally reflecting solar sail surface element of given area in function of the inclination angle are deduced.

Firstly, the force experienced by a surface due to the photon incident radiation is given by

$$F_i = PA(\cos\alpha)n_i \tag{2.2.1}$$

In contrast, the force experienced by a surface due to the photon reflecting radiation is provided by

$$F_r = -PA(\cos\alpha)n_r \tag{2.2.2}$$

Therefore, using the following vector identity

$$n_i - n_r = 2(\cos\alpha)^2 n \tag{2.2.3}$$

the total force vector exerted over an ideally reflecting solar sail surface is finally given by

$$F = PA(\cos\alpha)^2 n \tag{2.2.4}$$

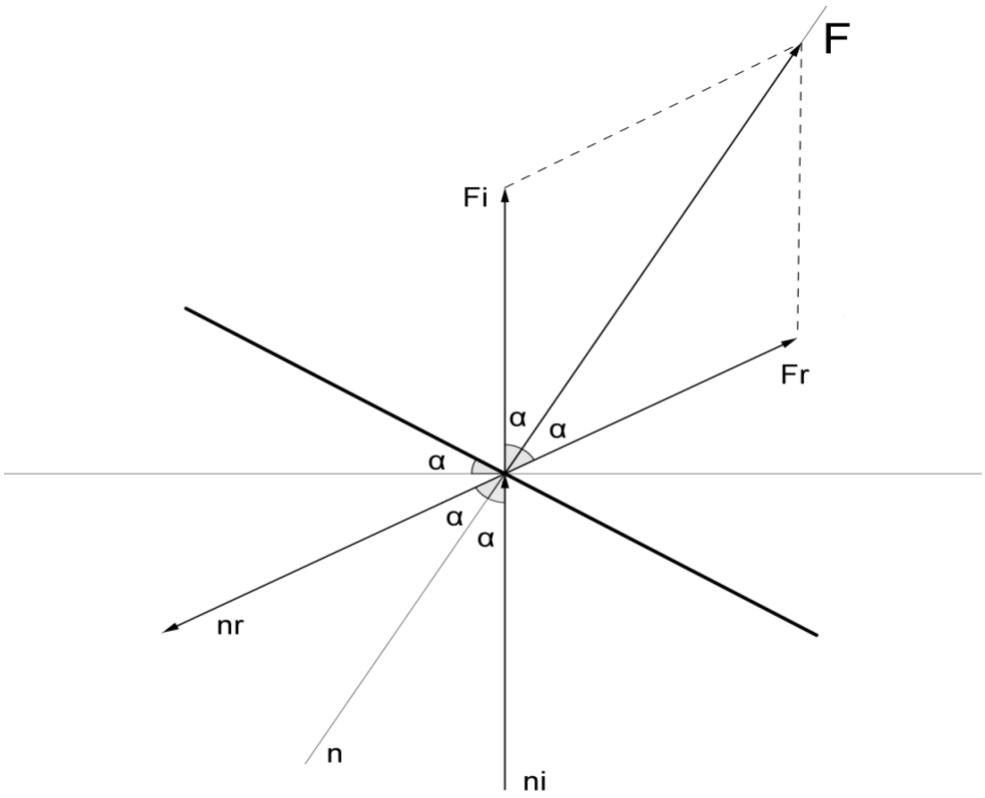

Figure 22 – Forces on an idealized surface element.

It should be noted that the angle α formed between the incident solar radiation vector and the sail normal vector is always equivalent to the one formed between the reflected solar radiation vector and the sail normal vector. Consequently, this angle corresponds to the sail pitch angle, i.e., the inclination angle formed between the sail surface and the horizontal axis, as it can be shown in Figure 22.

In terms of pressure exerted on an idealized solar sail surface, and considering that this is situated at the vicinity of the Earth, i.e. 1 A.U., equation (2.2.4) can be reformulated so that

$$P = 2\Psi_0(\cos\alpha)^2 \tag{2.2.5}$$

Since in this study, α may be regarded as the pitch angle, which refers to the deformed shape of a specific surface element described by a function w of r, the above equation may be given by the arctangent of the slope at a given point so that

$$P = 2\Psi_0\cos^2\left(\arctan\frac{dw}{dr}\right) \tag{2.2.6}$$

However, the above expression may be rewritten in a simplified expression, assuming the final form of

$$P = \frac{2\Psi_0}{1+\left(\frac{dw}{dr}\right)^2} \tag{2.2.7}$$

2.3 Analytical solution for a circular membrane under uniform transverse load

According to the information found in reference [26] an analytical method capable of determining a circular membrane´s mid-point maximum displacement, as well as its focal distance for the situation in which this is considered to be simply supported (translationally constrained) around its perimeter and subjected to a uniform pressure over one of its surfaces, has been established. A set of equations need to be derived for this specific situation. As it will be demonstrated, this derivation follows a strain-energy/virtual deflection approach, which is frequently used on problems of this nature. In order to obtain the final equations of interest, the computational software *Wolfram Mathematica® 7.0* was utilized as a support tool to carry out all the necessary calculations involved during this method. These are shown with more detail in Annex A.

Initially, the displacements of a circular membrane element for this particular case are described as

$$w = w_0 \left[1 - \left(\frac{r}{R}\right)^2\right] \tag{2.3.1}$$

$$u = r(R - r)(C_1 + C_2 r) \tag{2.3.2}$$

where w is the transverse displacement, w_0 the maximum transverse displacement, r the radial coordinate, R the radius of the circular membrane and u the radial displacement at radius r, whereas C_1 and C_2 represent two constants.

The radial and transverse strains are given respectively by

$$\varepsilon_r = \frac{du}{dr} + \frac{1}{2}\left(\frac{dw}{dr}\right)^2 \tag{2.3.3}$$

$$\varepsilon_t = \frac{u}{r} \tag{2.3.4}$$

Consequently, the strain energy U associated with stretching of the membrane may be rewritten as

$$U = \frac{\pi E t}{1 - \nu^2} \int_0^R ({\varepsilon_r}^2 + {\varepsilon_t}^2 + 2\nu\varepsilon_r\varepsilon_t) r dr \tag{2.3.5}$$

where E is the material´s Young modulus, ν its Poisson ratio and t the thickness of the membrane.

After the corresponding terms of the previous equation have been solved, the two constants C_1 and C_2 are found by imposing the requirements that

$$\frac{\partial U}{\partial C_1} = 0 \quad ; \quad \frac{\partial U}{\partial C_2} = 0 \tag{2.3.6}$$

This results that,

$$C_1 = -(-3w_0^2 + \nu w_0^2/4R^3) \tag{2.3.7}$$

$$C_2 = -(-3w_0^2 + \nu w_0^2/4R^4) \tag{2.3.8}$$

Next, the requirement that the change in work done W by a uniform transverse load P acting through a virtual displacement equals the change in strain energy associated with the virtual displacement is applied so that

$$W = 2\pi \int_0^R wPrdr \tag{2.3.9}$$

Since the total potential energy of an elastic body is given by the sum of the strain energy and the work done

$$\Pi = U + W \tag{2.3.10}$$

by imposing the following condition that

$$\frac{\partial \Pi}{\partial w_0} = 0 \tag{2.3.11}$$

an equation which allows obtaining the membrane´s mid-point maximum displacement is written in the form

$$w_0 = \sqrt[3]{\frac{3(1-\nu)PR^4}{(7-\nu)Et}} \tag{2.3.12}$$

Assuming that the deflection of the circular membrane matches a parabolic shape which in turn is given by the equation

$$w_f = \frac{r^2}{4f} \tag{2.3.13}$$

an expression which allows calculating the focal distance can also be obtained. The deflection of the previous equation is w_0 when $r = R$, thus it results that

$$f = \frac{R^2}{4w_0} \tag{2.3.14}$$

Finally, by substituting equation (2.3.12) into the preceding expression, the focal distance now assumes the form

$$f = \frac{1}{4}\sqrt[3]{\frac{(7-\nu)ER^2t}{3(1-\nu)P}} \tag{2.3.15}$$

2.4 Approximate focal distance of a circular membrane

In this chapter, a method capable of calculating the approximate focal distance of a given function $y = f(x)$ described by a determined number of pointsx_i, where $i = 1,n$ is presented. Firstly, the angles described by the functions curvature are determined at each node. This may be achieved according to the following equations:

$$\theta_i = atan\left[\frac{1}{2}\left(\frac{y_{i+1} - y_i}{x_{i+1} - x_i} + \frac{y_i - y_{i-1}}{x_i - x_{i-1}}\right)\right] \quad (2.4.1)$$

$$\theta_n = atan\left(\frac{y_n - y_{n-1}}{x_n - x_{n-1}}\right) \quad (2.4.2)$$

Next, the intersection of the light reflection vectors with a line corresponding to an initially assumed focal position y_{target} are calculated, through the given equation:

$$w_{fi} = \frac{1}{tan\left[-\frac{\pi}{2} + 2\theta_i\right]} \times (y_{target} - y_i) + x_i \quad (2.4.3)$$

In order to obtain the approximate focal distance described by the function´s curvature, the initial assumed focal position line y_{target} has to be adjusted so that the maximum value of the modulus of w_{fi} becomes a minimum. In other words, the solution is obtained when the focal plane which minimizes the radius size, maximum value of $|w_{fi}|$ representative of the smallest spot of reflected light, is found. Figure 23 illustrates this procedure.

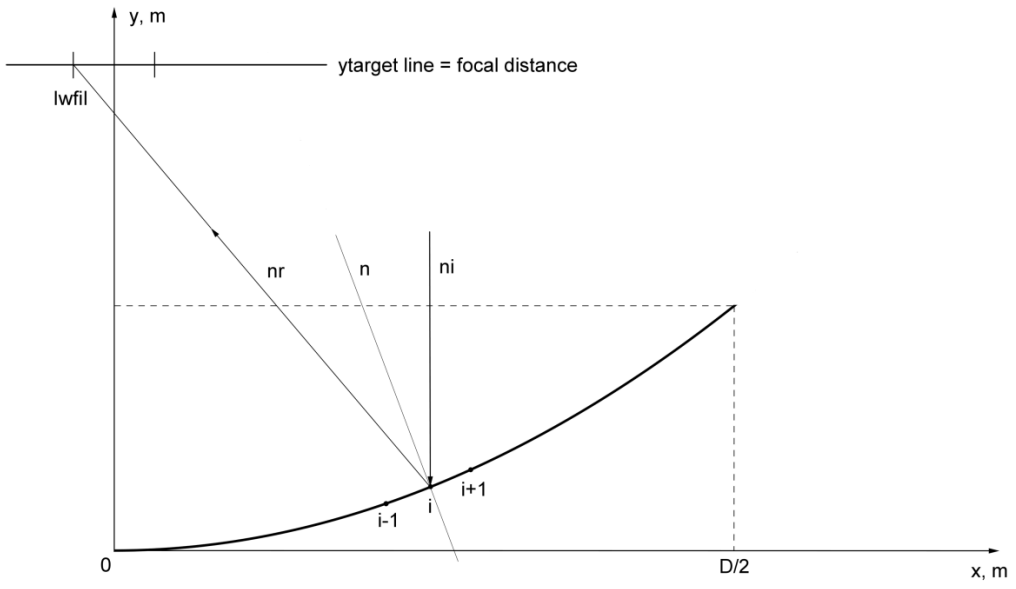

Figure 23 – Geometric focal distance and light spot radius determination

Chapter 3 – Initial studies with membrane-based components

Since all of the research is essentially based in a set of numerical analysis carried out using ABAQUS®, before moving on to the further advanced models used during the study, in this chapter, some primary simulations are first developed in order to gain further insight into the proper modelling of membrane-based structural parts using this specific FEM code. In particular, the different possibilities of modelling such structural components are analysed, discussed and compared. Additionally, experimental measurements are also conducted in the end, so as to validate the results obtained during some of the simulations performed.

3.1 ABAQUS® shell and membrane elements formulation

In the present case, the development of membrane-like structural parts is based on the definition of shell shape features, since these allow to model geometries in which one dimension, notably the thickness, is considerably smaller than the remaining ones. When it comes to the section definition type, there are however two distinct alternatives that allow defining very thin surfaces in space, namely homogeneous section types, which are used to assign section properties to a set of shell elements and membrane section types, used to assign section properties to a set of membrane elements.

According to the established section definition type, the respective element type families (membrane or shell) also need to be later specified when generating the mesh. Generally speaking, membrane elements are characterized by ultra-thin surfaces that are only able of offering strength to in-plane tension loads, since these do not have any bending or transverse shear stiffness. In the case of shell elements, the only difference is that some degree of bending stiffness will be actually present. Figure 24 gives an illustration of two shell/membrane elements, quadrilateral (four nodes) and triangular (three nodes). SPOS represents the top face of the element (positive normal direction) while SNEG is the opposite face of the element.

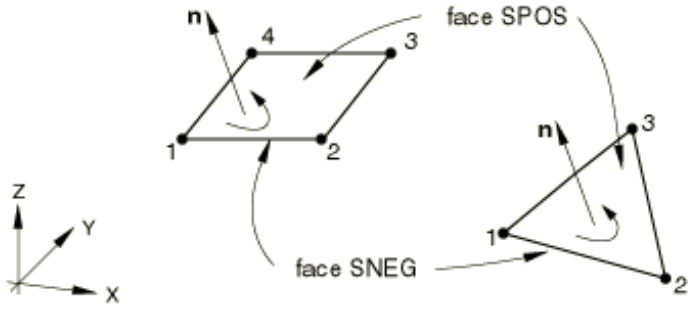

Figure 24 - General shell/membrane elements with respective faces [27].

3.2 Square membrane under uniform pressure

Given the previous concepts, a 20 cm side square membrane part is initially considered for simulation purposes. The idea is to determine the maximum displacements in its middle point caused by the single effect of a normal distributed load representative of solar pressure magnitude over a perfectly reflecting surface ($9.12E^{-6}$ N/m^2) for all the available element type families of different geometric orders and with specific given boundary conditions.

3.2.1 Numerical model description

The material elected for the study model is Mylar®. According to the information found in some manufacturer´s datasheets [28, 29], an average approximate value of 3.5GPa is stipulated for the Young modulus, 0.38 for the Poisson ratio and 1350 kg/m^3 for the density. These properties are defined to the model´s section as an isotopic material. During the simulations, two different element families (membrane and shell) of two respective geometric orders (linear and quadratic) are considered:

- **M3D4:** A four node three dimensional quadrilateral membrane
- **S4:** A four node doubly curved general-purpose shell
- **M3D8:** An eight node three dimensional quadrilateral membrane
- **S8R:** An eight node doubly curved thick shell with reduced integration

The last considered element presents a different level of integration in relation to the others. In fact, being the only type of quadrilateral shell element from quadratic order available in ABAQUS®, this uses reduced-integration, while the other ones use full integration. The difference between these two approaches resides on the number of points required to integrate the polynomial terms in the element´s stiffness matrix. Generally speaking, full integrated linear elements, such as M3D4 and S4, use an array of two integration points in each direction, while the quadratic ones, including M3D8, use three. As for the reduced integration elements, a fewer integration point is used in each direction in comparison to the full integrated ones. In this regard, reduced-integration quadratic elements, like S8R, use an array of two integration points across each direction instead of three.

Some additional features such as ABAQUS® *NLGEOM* option on the Step definition module need to be specified in order to conduct the simulations accurately. The inclusion of this feature will be further discussed in the following chapter. Since a stress-free flat membrane has no stiffness normal to its plane, if the normal solar pressure load is directly applied to the model the simulation fails due to numerical singularities and convergence difficulties. To counteract this effect, membrane elements necessarily have to be initially submitted to some

sort of plane stress state which can be achieved for instance by submitting its edges or nodes to force fields or small displacements. This pre-tension across the edges would have not been necessary for the case of shell homogeneous elements, however, this is anyway considered so as to compare the results of the simulations for both family element types under the same conditions. In this regard, during the following simulations the upper and right edges are submitted to different values of small displacements across the *x* and *y* axes respectively in order to pre-stress the membrane. The remaining left and bottom edges are kept translationally constrained with respect to the *x* and *y* axes whereas all the edges are translationally constrained across *z* axis (Figure 25).

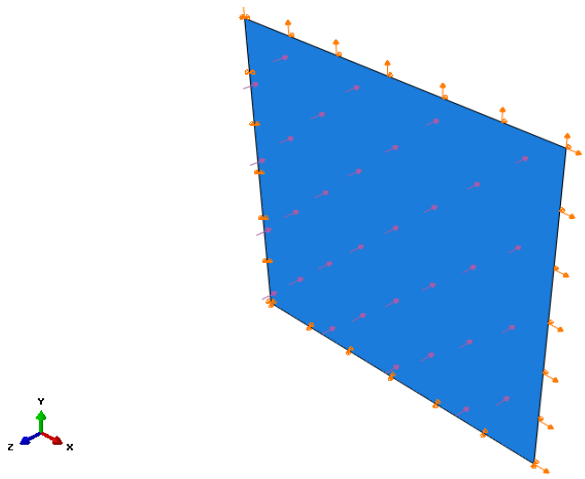

Figure 25 - 20 cm side square membrane with loads and boundary conditions.

3.2.2 Results and discussion

The mid-point maximum deformations for a film of thickness 2.5μm, considering different pre-displacement magnitudes are presented in Table 1.

Table 1 - Middle-point deformations considering different membrane and homogeneous shell elements for different pre-displacement magnitudes.

Pre-displcament [m]	M3D4 disp[m]	S4 disp[m]	M3D8 disp[m]	S8R disp[m]
$5.00E^{-7}$	$-7.63228E^{-07}$	$-7.63221E^{-07}$	$-7.61720E^{-07}$	$-7.61677E^{-07}$
$1.00E^{-7}$	$-3.81047E^{-06}$	$-3.80962E^{-06}$	$-3.80293E^{-06}$	$-3.80196E^{-06}$
$5.00E^{-8}$	$-7.54394E^{-06}$	$-7.54048E^{-06}$	$-7.52885E^{-06}$	$-7.52520E^{-06}$
$1.00E^{-8}$	$-2.38664E^{-05}$	$-2.38636E^{-05}$	$-2.38071E^{-05}$	$-2.37994E^{-05}$
$5.00E^{-9}$	$-2.83038E^{-05}$	$-2.83185E^{-05}$	$-2.82276E^{-05}$	$-2.82355E^{-05}$
$1.00E^{-9}$	$-3.20283E^{-05}$	$-3.20239E^{-05}$	$-3.19340E^{-05}$	$-3.19248E^{-05}$
$5.00E^{-10}$	$-3.24846E^{-05}$	$-3.24858E^{-05}$	$-3.23873E^{-05}$	$-3.23847E^{-05}$
$1.00E^{-10}$	$-3.28484E^{-05}$	$-3.28543E^{-05}$	$-3.27483E^{-05}$	$-3.27517E^{-05}$
$5.00E^{-11}$	$-3.28938E^{-05}$	$-3.29003E^{-05}$	$-3.27933E^{-05}$	$-3.27975E^{-05}$
$0.00\ E^{0}$	Simulation fails	$-8.59746E^{-05}$	Simulation fails	$-8.62480E^{-05}$

From the results obtained during the first simulation it becomes obvious that as the pre-displacement magnitude decreases, the higher the mid-point maximum deformations turn out to be, being that the minimum positive pre-displacement value necessary to avoid numerical problems, and therefore a failed simulation, is 5E-11 m. Furthermore, it is possible to conclude that no matter the element types adopted, the resulting maximum deformation values are very similar for the same magnitude of pre-displacement. Indeed, if a fine mesh is defined, as in this case where the model adopts 400 *quadrilateral-dominated* elements (Figure 26), the different element geometric orders and levels of integration are not considered to influence much the results precision for the case of shell shape parts.

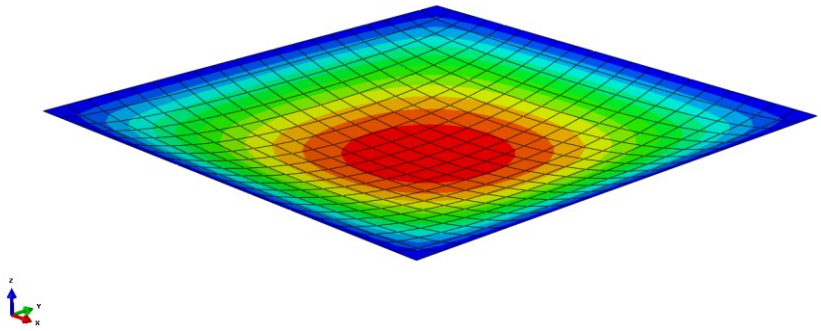

Figure 26 - Deformation field obtained for the numerical model.

A second simulation was also carried out with the same model, this time considering a variable section thickness whereas the pre-displacement magnitude assumed a fixed value of $1.00E^{-7}$ m. The obtained results can be visualized in Table 2.

Table 2 - Middle-point deformations considering different membrane and homogeneous shell elements for different thickness values.

Thickness [m]	M3D4 disp[m]	S4 disp[m]	M3D8 disp[m]	S8R disp[m]
$1.00E^{-7}$	$-6.56723E^{-05}$	$-6.56844E^{-05}$	$-6.55128E^{-05}$	$-6.55126E^{-05}$
$1.00E^{-6}$	$-9.45348E^{-06}$	$-9.45355E^{-06}$	$-9.43462E^{-06}$	$-9.43425E^{-06}$
$1.00E^{-5}$	$-9.53949E^{-07}$	$-9.50058E^{-07}$	$9.48167E^{-07}$	$-9.52064E^{-07}$
$1.00E^{-4}$	$-9.54037E^{-08}$	$-6.35218E^{-08}$	$-9.52152E^{-08}$	$-6.34403E^{-08}$
$1.00E^{-3}$	$-9.54038E^{-09}$	$-1.71006E^{-10}$	$-9.52153E^{-09}$	$-1.71629E^{-10}$
$1.00E^{-2}$	$-9.54004E^{-10}$	$-1.82179E^{-13}$	$-9.52153E^{-10}$	$-1.82970E^{-13}$

According to the results obtained during the second simulation, it is possible to verify that the difference for the mid-point maximum deformations between membrane element and shell element types becomes more pronounced as the thickness of the film increases. This effect may be explained due to the influence of the bending stiffness, which is greater as the second moment of area increases. However, if a higher degree of pre-tension had been settled, this

divergence would not have been so high for the cases where greater values of thicknesses were considered. As it will be seen in the following chapters, the material used for the solar sail´s membranes is typically compromised between 1μm to 10μm, which is still in the range where the differences of the maximum deformations obtained for the four types of elements are practically negligible.

3.3 Rectangular membrane under concentrated load

In this section, experimental measurements were conducted in order to compare the results verified for the real behaviour of some distinct types of membrane films with the ones obtained numerically. Another numerical simulation was also carried out for this purpose.

3.3.1 Experimental setup

During the experimental procedure, the top side of a 20cm × 15cm side Mylar® sample was initially clamped in a wooden frame, which in turn was hanged to a rigid support structure as it can be visualized in Figure 27.

Figure 27 - Experimental setup to pre-tension the membrane [30].

With the purpose of achieving some degree of pre-stress and to avoid the formation of wrinkles, a small weight was added to the bottom side of the Mylar® film as a stipulated line load. This needs to be considered during the parallel FEM analysis in order to conduct the simulations for the cases where membrane element types are adopted. In this stressed condition, the bottom edge of the experimental model was also clamped in the wooden frame, while the two other edges remained free. After the film has been imposed to these boundary conditions, the wooden frame was then placed horizontally over a laser sensor used

to measure the vertical displacements in the middle part of the membrane, as it can be demonstrated in Figure 28.

Figure 28 - Displacement measurement with a laser sensor device [30].

Once it would be unpractical to submit the experimental model to a distributed pressure of magnitude corresponding to the one of solar radiation, in this case, coins were positioned on the middle part of the film as a form of weight instead. By doing so, measurable deformations could be achievable on the film samples. In total, five step measurements (as more coins were added) were performed on three different types of Mylar® of various thicknesses:

- **Mylar® 850** (20μm)
- **Mylar® OL 140L** (13μm)
- **Non-specified type of Mylar®** (5μm)

3.3.2 Numerical model description

Regarding the numerical model, after the corresponding measurements have been correctly established, a small circular partition of radius corresponding to the one of a coin (1 cm) is defined on the model´s central part. In order to compare the obtained results in relation to the experimental model, different uniform pressure values corresponding to the weight of the coins needed to be applied over this partition. The pressure magnitudes for the five step measurements performed are found in Table 3.

Table 3 - Pressure magnitudes as a function of growing number of coins.

Number of coins	Mass [Kg]	Weigh [N]	Pressure [N/m^2]
2	0.014	0.13734	437.2
3	0.0218	0.213858	680.7
5	0.0374	0.366894	1167.9
7	0.053	0.51993	1655.0
12	0.0905	0.887805	2826.0

Similarly to what is verified for the experimental model, one of the film´s shorter edges stays translationally constrained across all the directions, while the two longer ones remain free. As for the opposite shorter edge, this one is submitted to a small amount of pre-tension across the *x* axis. It was verified that a small pre-displacement of $3.24E^{-6}$ m would lead to a good approximation of the load effect stipulated on the experimental model. However this boundary condition only becomes valid when the membrane element type is to be considered. Since a shell element type without being submitted to any degree of pre-tension is also here considered, in this situation, both shorter edges remain translationally constrained.

The two element families resorted during these simulations were both of geometric linear order, namely:

- **M3D3:** A three node triangular membrane
- **S3:** A three node triangular general-purpose shell

Some important aspects such as the material properties adopted and the ABAQUS® *NLGEOM* option remain unchanged compared to the previous numerical simulations.

3.3.3 Results and discussion

Figure 29 illustrates the mesh topology adopted together with the resulting deformation field for an arbitrary state as the coins are placed on the middle part of the film. As it can be seen, for this simulation the mesh is based on a free technique composed by a total of 490 *trilateral* elements. These type of elements turn out to be more suitable for irregular geometries, as it happens in this case for the circular edges that define the model´s middle partition. A higher number of elements also needed to be specified around this area, in order to obtain a more consistent mesh for the whole model.

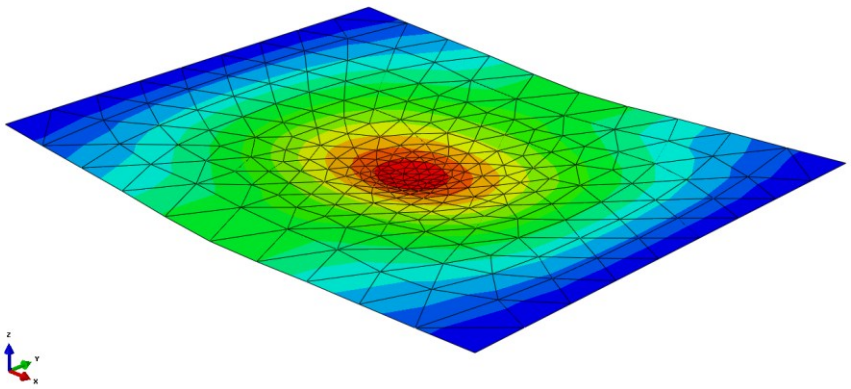

Figure 29 - Mesh and deformation field verified for the numerical model.

The plot of Figure 30 shows the results corresponding to the variation of the mid-point maximum displacements verified for the thickest film (Mylar® 850 of 20μm) obtained both experimentally and numerically. It is possible to observe that as more weight was introduced (growing number of coins) the displacements obtained from the numerical simulations, no matter the element type adopted, are always higher than those of the experimental measurements. This could be explained probably due to imprecise material properties used as the numerical models data input, since there have been some difficulties in ascertain the exact values of the Young modulus for each of the different types of Mylar® samples considered on the experiment. For this reason, the same properties previously mentioned were assumed during all the numerical simulations, since they are average representatives of the different types of Mylar® materials. Nevertheless, despite the divergence verified for the displacements obtained experimentally and numerically during the five step measurements, both curves present a similar growing trend. Therefore, an accurate representation of the section properties defined as isotropic materials during the FEM analysis gives a good approximation to the real behaviour of such types of structural parts. The plots regarding the mid-point displacement results for the other Mylar® samples are found in Annex B. Here, it is possible to conclude that during this investigation the divergence observed between the experimental measurement and numerical simulation curves is more evident for the 5μm Mylar® sample and not as significant for the 13μm Mylar® OL 140L film.

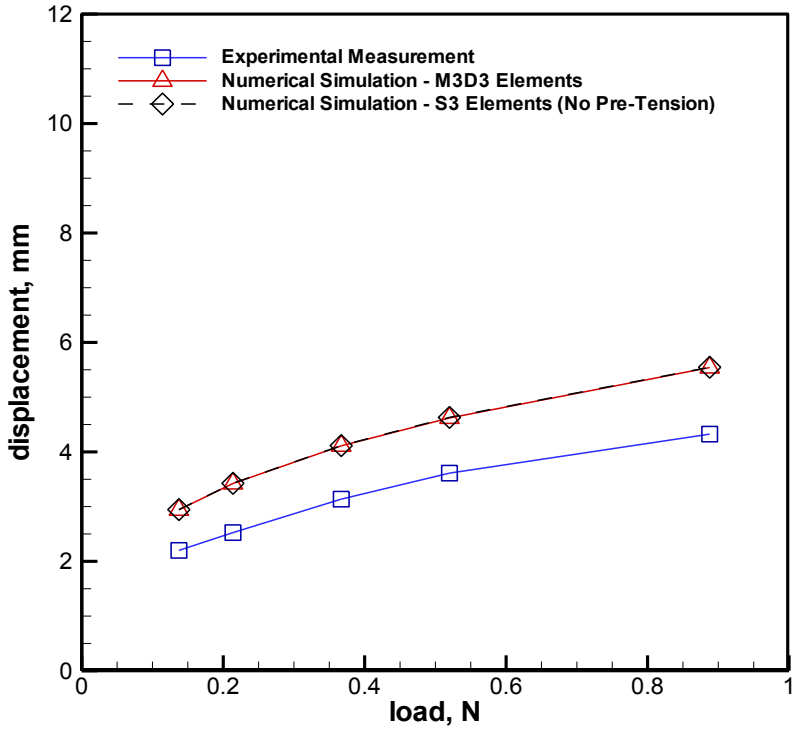

Figure 30 - Experimental and numerical results of mid-point displacements verified for Mylar® 850 of 20μm film.

Chapter 4 – Flat circular membrane under solar pressure

In this chapter, a structural concept which relies upon the exclusively use of a flat circular Mylar® made membrane without any type of load carrying elements along its radials, such as conventional longitudinal booms, is suggested. For this situation, since the solar pressure inevitably causes some deformations on any rigid body, the possibility of the structure in resorting to this loading condition as a means of obtaining an intended parabolic curvature during its operating phase is explored. In addition of having a less complex deployment mechanism, this concept would also be highly advantageous in terms of a lower final weight of the structure. With the purpose of validating this design, namely to assess it parabolic shape accuracy, i.e., the degree to which the actual resulting shape deviates from the intended parabolic shape, a parametric study is performed aimed at estimating several parameters of interest, such as the resulting deformed coordinates, together with the approximate focal distances and respective light spot diameters on the focal plane as well as the structure's light concentration capacity. A total of sixteen simulations are carried out considering four different radius sizes of the circular geometry, namely 1m, 5m, 10m and 25m, each of which for four different thicknesses of the Mylar® material, in particular 1μm, 2μm, 5μm and 8μm, in order to compute this variables.

4.1 Numerical model formulation

The development of the numerical model´s membrane-like circular structural part is based on the definition of a shell shape feature, the same way as it has been previously demonstrated in Chapter 3. The geometry is assumed to be axisymmetric with the symmetry axis directed towards the Sun, i.e., collinear to the incoming sunlight flux direction. As for the section definition type, shell homogeneous elements are selected as these proved themselves to be the most feasible ones in comparison to the membrane type elements, given the sizes and thicknesses of the geometrical models here adopted. By considering membrane elements, most of the simulations would fail due to convergence difficulties as a result of the extremely large dimensions of very thin sections. Additionally, a pre-tensioning strategy would also have to be necessarily established, which would simultaneously make the analysis more complex and more susceptible to result inaccuracies. Regarding the boundary conditions, the membrane remains simply supported (translationally constrained) around its perimeter during all the simulations (Figure 31), so that it is allowed to deflect around its periphery and hence achieve a curvilinear shape of a single concavity. Mylar® (brand trademark for polyester film) is the material elected due to its lightweight and resistance to moderate temperatures,

where the same average values of 3.5GPa for the Young modulus, 0.38 for the Poisson ratio and 1350 kg/m^3 for the density are again attributed to the section as an isotopic material.

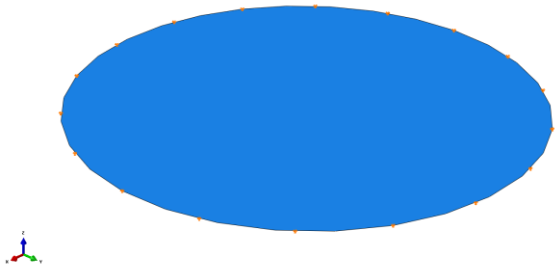

Figure 31 - Numerical model with respective boundary condition.

Since the main focus of the study is to evaluate the structure´s long term response to the applied solar pressure load, a *Static General* type of analysis is specified on the ABAQUS® Step module. Once more, the *NLGEOM* feature needs to be taken into consideration due to the expected geometrically nonlinear behaviour of the structure. A nonlinear type of analysis is characterized by a significant change in the structure´s stiffness as it deforms, which may arise as a consequence of its geometry, material properties or boundary conditions. Therefore, contrary to the assumption of a linear analysis where the stiffness matrix only needs to be assembled once, in a nonlinear analysis the stiffness matrix has to be assembled and inverted many times through an iterative process, thus making the course of the analysis much more complex to solve than the linear analysis in order to obtain result precision.

Regarding the nonlinear geometric behaviour of a structure, which is related to changes in stiffness as a result of its shape modification, even though this normally arises as result of very large deformations, such shape-caused changes in stiffness may also occur when the deformations are small, as it happens for the present numerical model. In this case, when the membrane is initially flat, it resists to the solar pressure load only due to its bending stiffness. However, as it starts to get deformed, since the film inevitably stretches, according to Hook´s law the resulting strains generate additional in-plane membrane stiffness (Figure 32), thus making the membrane much stiffer than the predicted by linear analysis.

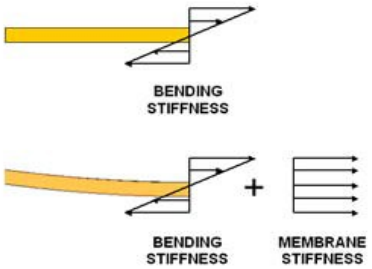

Figure 32 - Stiffness for initially flat and for deformed membrane [31].

4.1.1 Mesh convergence study

The numerical model assumes a sweep generated mesh technique composed of several *quadrilateral-dominated* S4 elements. Prior to initiate the parametric study, a mesh convergence study is performed on the 1m radius membrane of thinnest material (1μm) in order to ascertain the adequate mesh refinement, representative of a good compromise between result accuracy and computation time. Such task is focused on the membrane´s maximum deformations localized at its middle point, as a result of a uniform pressure load applied over its surface and under a nonlinear equilibrium state. A total of eleven models of increasing mesh fidelity are considered, where the number of increasing elements are manually defined across the membranes circular perimeter as well as through its radials. The obtained results for each of the considered models may be found on the plot of Figure 33.

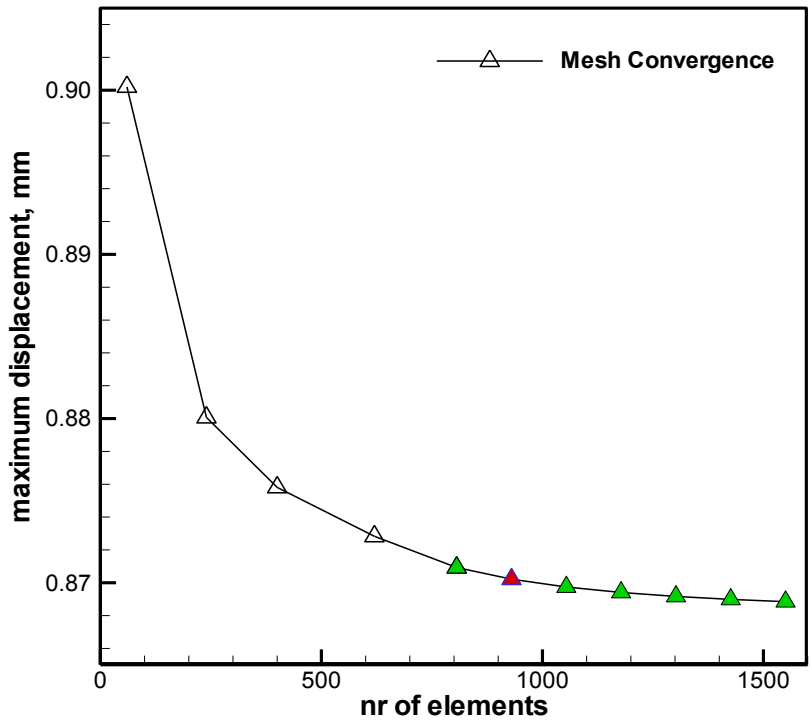

Figure 33 - Mesh convergence study results with S4 elements.

Since the curvature profile described by the resulting deformation function is expected to be more pronounced towards the model´s central part, a higher number of nodes should be specified in this region in order to accurately interpolate it. For this reason, starting from the model which accounts a total of 806 elements (green triangles of Figure 33), all the models assume a bias ratio of 3 towards the central node across the radials. After completing all the simulations, it was found that a mesh composed by a total of 930 elements (red triangle of Figure 31) proved to be sufficiently accurate and relatively efficient in terms of computation time. In fact, the error obtained between this model´s maximum deformation and the one

considered previously is less than 0.1%, and thus practicably negligible. Figure 34, shows the model´s final mesh adopted for the subsequent realization of the parametric study. It is established with 62 elements around its perimeter and 15 elements with a bias ratio of 3 towards the central node across the radials, which all together thus form 930 S4 elements.

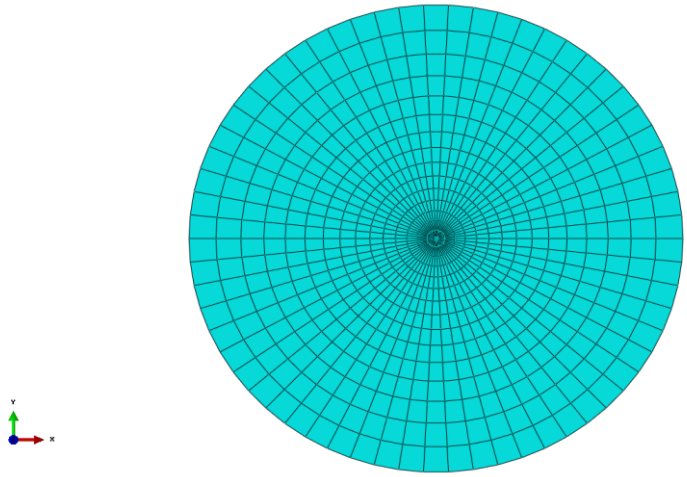

Figure 34 - Mesh adopted for the numerical model.

4.1.2 Solar pressure loading conditions

Since the circular membrane is assumed to be perfectly aligned towards the incoming sunlight flux, for the situation when it is considered to be initially flat, the solar pressure over its surface has a uniform distribution (Figure 35). However, if the final deformed shape becomes sufficiently pronounced, it should be noted that a new distribution inevitably arises as the slope of the membrane increases, thus making it necessary to change the loading properties of the resulting pressure after each deformation increment for every of the membrane´s mesh elements (especially to the ones which are closer to the circular outer edge).

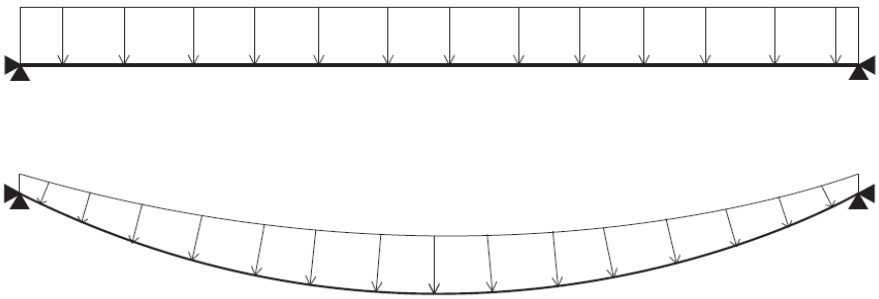

Figure 35 - Pressure distribution over flat and deflected circular membrane [30].

Although the resulting deformations are expected to be extremely small as consequence of the solar pressure´s very low magnitude, this iterative procedure is even so taken into

account for the numerical simulations during this study. In this case, the model´s geometries of various radius sizes, material properties as well as the assigned mesh are first defined trough the ABAQUS® functionalities in order to generate the input file named *circular.inp* which contains all of this information in detail. However, since ABAQUS® alone does not allow changing the loading properties during every step increment, a routine entitled *circular.m* is created in MATLAB® for this purpose, which in turn is coupled with the ABAQUS® job processor for running the analysis. The code, referring to the 1m radius membrane case, may be found in Annex C. For larger sizes, the radius parameter has to be adapted on the code.

4.2 Results and discussion

After the code has been executed, some initial files, namely a *step.txt* file which in turn is specified in the end of the *circular.inp* input file, together with a *data.txt* are firstly created for writing and reading purposes. Next, as a first interaction step, the resulting pressure is uniformly applied over the membrane´s surface. Here, the MATLAB® code starts by running the *circular.inp* input file and after that a PYTHON® script (*output.py*) in order to write the coordinates of the deformed membrane in the file *data.txt*. For the following iterations, the *data.txt* file is read by the MATLAB® *circular.m* code and a polynomial function of degree 6 which matches the deformed membrane´s coordinates at the correspondent nodes is created. Figure 36 shows an example of the final obtained function regarding the 1m radius of 1μm thickness deformed membrane provided by MATLAB®.

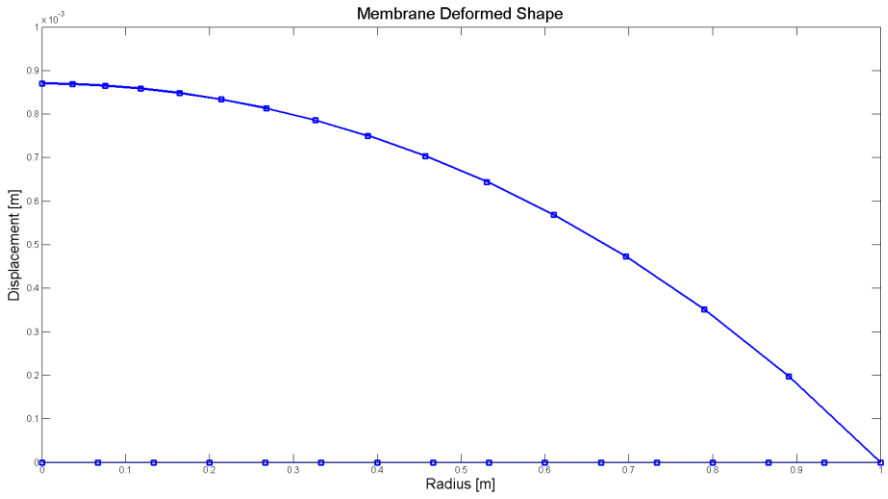

Figure 36 – Final solution for the 1m radius/1μm thickness membrane supplied by MATLAB®.

Consequently, the slopes are calculated at each node and out of these the resulting pressure magnitudes applied for each element. It is assumed that the slope of a given element is characterized by the mean value between the slopes of two of the nodes along the radials

which form that respective element. As it should be noted, this calculation is achieved with reference to equation 2.2.6. Lastly, the code writes a new *step.txt* containing the new pressure distribution data and runs the *circular.inp* file again until the relative error between the two last obtained functions is smaller than a maximum stipulated value. Figure 37 gives a general idea of sequence related to this procedure.

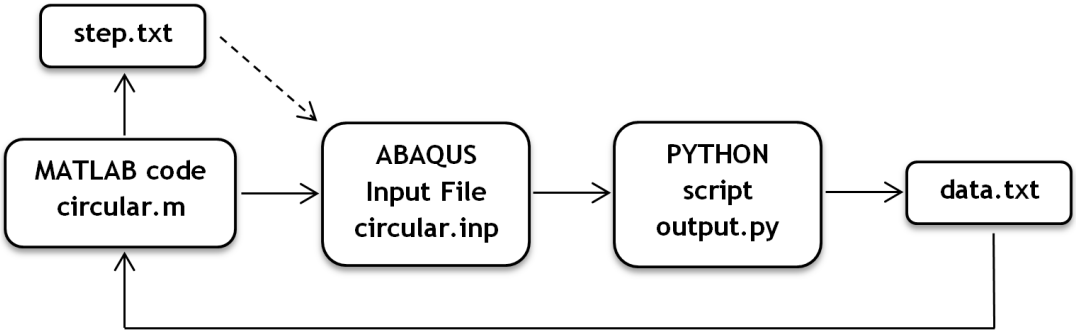

Figure 37 - Numerical analysis process scheme during the parametric study.

Some additional parameters such as the initial step increment sizes as well as the maximum number of increments also had to be adjusted in the code for each of the sixteen simulations in order to obtain convergence of the solutions. A maximum number of 500 increments were considered in all the simulations, while the initial increment sizes varied between $1E^{-25}$ for the smallest membranes and $1E^{-08}$ for the larger ones. At the end of each analyse, an output file (*circular*.odb) is also created which allows interpreting the obtained results graphically on the ABAQUS® environment. Figure 38 shows an example of the displacement field in meters obtained for the case of the 1m radius of 1μm thickness membrane (the deformation scale factor has been relatively exaggerated in order to give a better understanding of the final deformed shape). As expected, the deformations increase towards the centre of the membrane, being maximal on its middle node for all the situations considered.

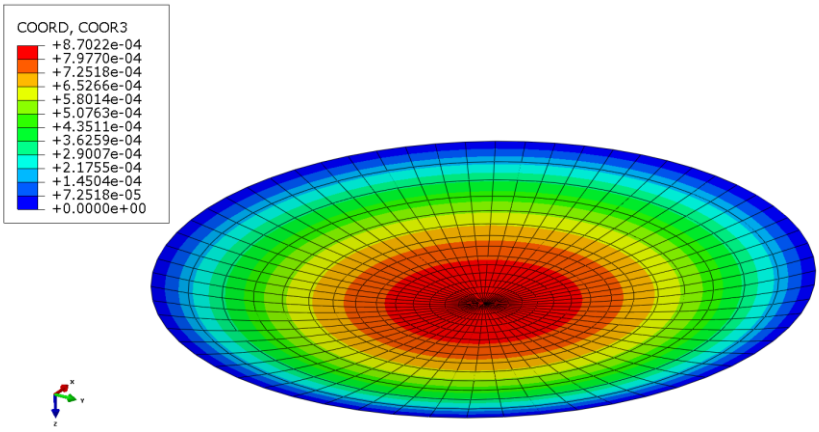

Figure 38 - Circular membrane deformation field under non-uniform pressure load.

4.2.1 Nodal displacements

After the analyses have been successfully completed, the nodal displacements across the membrane´s normal axis are obtained for the sixteen cases of varying radius size and material thickness. The plot of Figure 39 shows the non-dimensional displacements along the radial position for all the four radius sizes considered with respect to the 1μm thickness membrane. It is evident that the membrane´s deformations are always maximal for the middle node and that they increase for the cases of higher radius values. The plots concerning the remaining thicknesses adopted for the material can be found in Annex D.

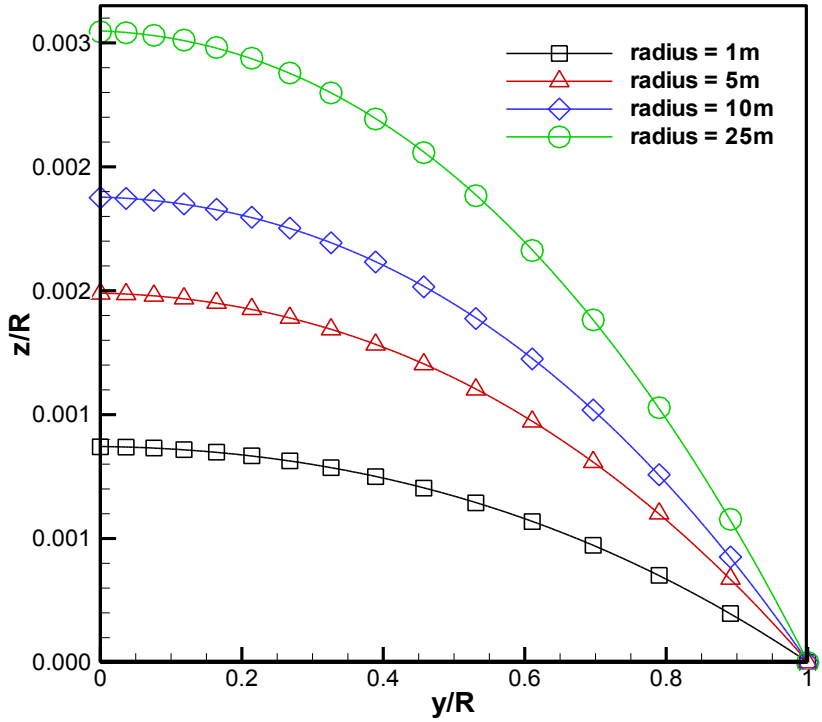

Figure 39 - Non-dimensional displacement variation for the 1μm thickness membranes.

The plot of Figure 40 illustrates the absolute middle point displacements in meters, w_0 as a function of the radius size for the four thicknesses considered, obtained both numerically (under non-uniform pressure load) and analytically (under uniform pressure load) with accordance to the theorem presented in Chapter 2.2.3. The maximum value of w_0 is related to the case of the highest radius (25m) with the thinnest material (1μm), whereas it becomes minimal for the smallest radius (1m) with the thickest material (8μm). Consequently as it can be seen, the middle point deformation grows as the radius size is increased and decreases with the increase of the thickness. Furthermore, the analytical expression regarding w_0 always provides higher values when compared to the ones obtained numerically with a mean approximate error of approximately 3.43%. Finally, the maximum error regarding the middle node displacements obtained numerically for the membrane subjected to an iterative

pressure calculation, i.e., through the MATLAB® routine, and by a simply uniform pressure magnitude, whose solution can be determined solely by resorting to ABAQUS®, is found to be less than 10^{-4} % and therefore practically negligible.

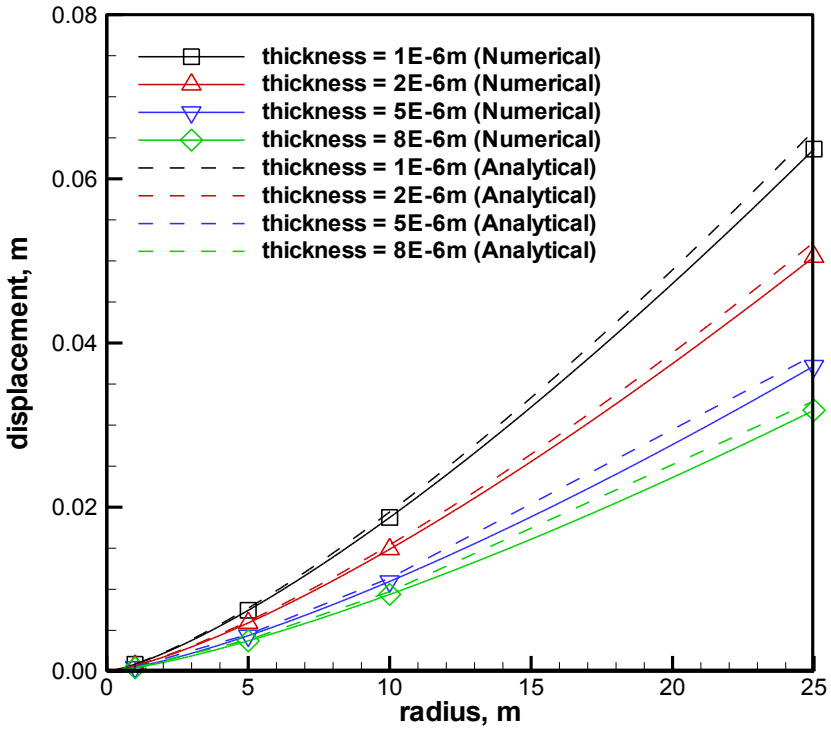

Figure 40 - Middle point displacement variation with membrane radius *R* and thickness *t*.

Based on the numerical results, for these specific material properties an expression capable of representing the middle point displacement variation is derived for every combination of membrane radius *R*, and membrane thickness *t*. This relationship is given by following equation in which all quantities are represented in meters:

$$w_0 = 8.702 \times 10^{-6} R^{\frac{4}{3}} t^{-\frac{1}{3}} \tag{4.1}$$

In this case, the maximum error regarding the middle point displacements obtained during the numerical simulations and as given by this equation is 0.02%.

4.2.2 Parabolic approximations

In order to assess how different the deformed membrane shapes under the influence of solar pressure are from true parabolic surfaces, second degree polynomial functions are fitted to the data corresponding to the obtained displacement profiles. Such accomplishments are

guaranteed by resorting to the *Microsoft Excel® 2010* software. For simplicity reasons, here the nodal deformation coordinates are manipulated so that the respective functions exhibit a positive concavity instead, with the central node (maximum deformation point) coincident with the origin of the reference frame. Since the membrane´s deformations are symmetric, the obtained deformed coordinates across its radials are mirrored, so that the entire curvatures may be outlined, i.e., across the membrane´s diameter. By doing so, trend lines of second order polynomial types are then attributed to the complete deformation curvatures with an interception specified for the middle node (origin) in order for these to be symmetric. The plot of Figure 41 gives an example for the case of the 25m radius of 1μm thickness membrane. As it may be seen, these assessments clearly show that the real deformations are not perfect paraboloids even though they resemble ones.

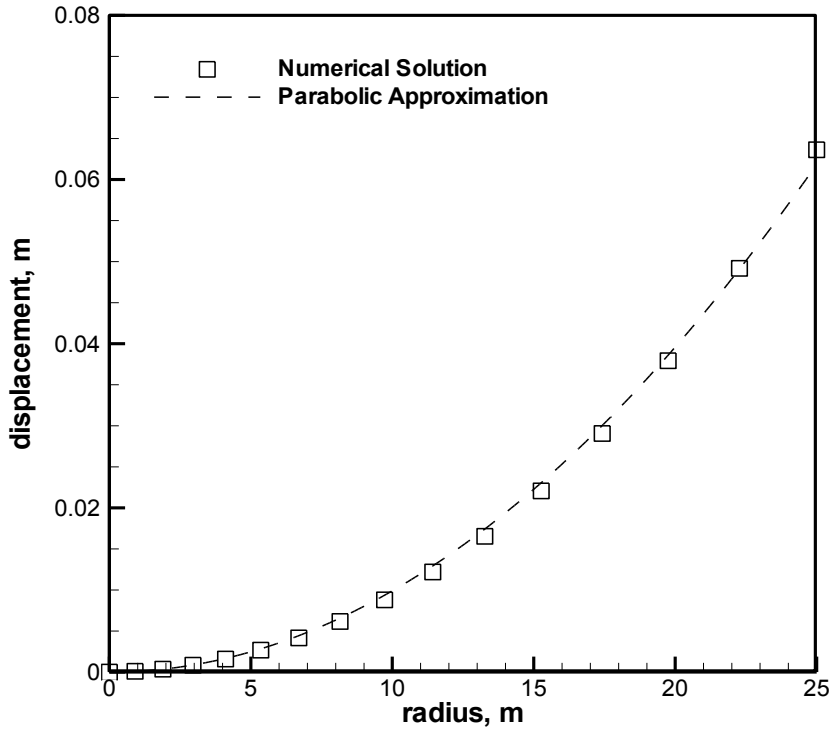

Figure 41 - 25m radius/1μm thickness membrane deflection and respective parabolic fit.

Consequently, the absolute mean percentage errors between the real deformed membrane shapes and the parabolic fits are also computed according to equation 4.2

$$M = \frac{100\%}{n}\sum_{t=1}^{n}\left|\frac{Y_r - Y_p}{Y_r}\right| \tag{4.2}$$

where n represents the number of nodes considered, in which case are 15 (excluding the middle node), Y_r the real deformed coordinates obtained numerically and Y_p the deformed coordinates referring to the parabolic fit functions. Table 4 shows the obtained results for all

simulations performed during the parametric study. According to these, it is possible to conclude that all of the resulting deformations are indeed very close to parabolic ones, and that even though the mean percentage errors generally tend to increase with the increase of radius and decease with the increase of thickness, these variations are not very significant. Therefore, for this range of radius and thicknesses values, the resulting deformations under the same pressure magnitude are not considered to have a strong impact on the shape accuracy of the membranes. Nevertheless, the maximum mean percentage error is verified for the case of the highest radius (25m) with the thinnest material (1μm), whereas the minimum occurs for the case of the smallest radius (1m) with a material thickness of 5μm.

Table 4 - Parabolic fit absolute mean percentage errors.

	Thickness [μm]			
Radius [m]	1	2	5	8
1	4.919%	4.486%	4.400%	4.488%
5	5.223%	5.195%	4.919%	4.601%
10	5.228%	5.223%	5.168%	5.039%
25	5.229%	5.228%	5.223%	5.210%

4.2.3 Focal distances

The deformed coordinates obtained from the numerical analysis at the discrete radial positions are used to estimate the approximate focal distances. Since the deformed shapes are not exactly parabolic surfaces, they are not able to concentrate the solar light at a single focal point. Therefore, in a more general sense, here the geometric focal distance is defined as the distance along the symmetry axis from the origin of the deformed shape to the focal plane, i.e., the plane orthogonal to the symmetry axis of the membrane that minimizes the radius size of the correspondent smallest light spot. Based on the principle presented in Chapter 2.2.4, an optimization routine has also been developed resorting to *Silverfrost Fortran® 95 Express* for this purpose. The code, concerning the 1m radius membrane of 1μm thickness case, is divided in three distinct source files which may be found in Annex E. It should be noted that the y_{target} (initial assumed focus position) parameter has to be adjusted during each simulation in order to find desired approximate solution.

The plot of Figure 42 describes the focal distance variation in meters, f, as a function of the radius for the four thicknesses considered, obtained both geometrically, as a result of the pressure iterative calculation with reference to the criterion presented in Chapter 2.2.4, and analytically (under uniform pressure magnitude) again with the same theorem reported in

Chapter 2.2.3. In the latter, the focal distance is calculated assuming a true parabolic deformed shape. The maximum focal distance is computed for the case of the highest radius (25m) with the thickest material (8μm), whilst the lowest focal distance is verified for the case of the lowest radius considered (1m) with the thinnest material (1μm). As it happened previously with w_0 the focal distance also grows as the membrane radius is increased although oppositely with respect to the thickness, i.e. in this case, the focal distance decreases with reducing thickness. Once again, the analytical expression regarding f also provides higher values when compared to the ones obtained with the geometric approach however, this time with an inferior mean percentage error of approximately 0.53%.

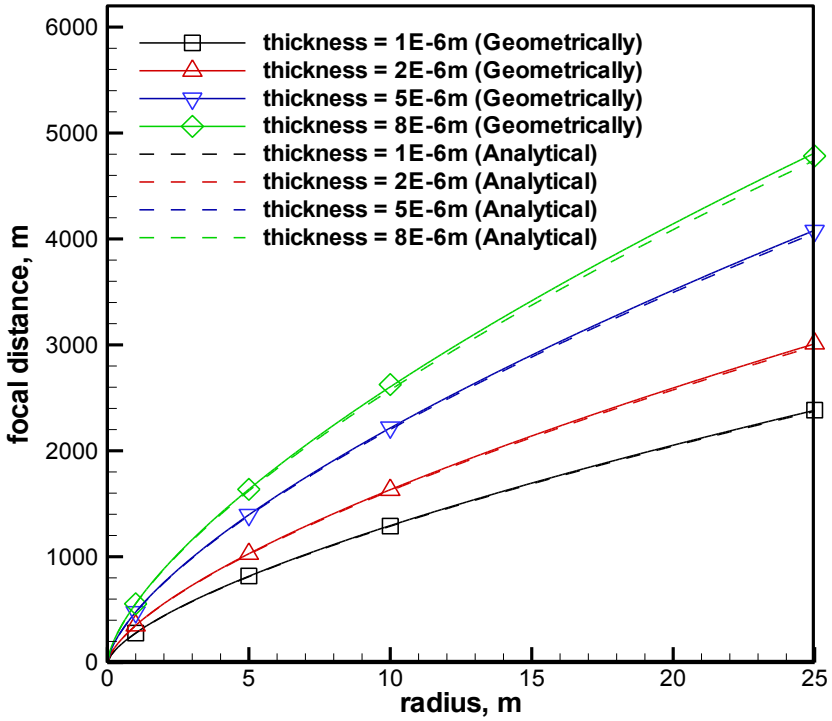

Figure 42 - Focal distance variation with membrane radius *R* and thickness *t*.

According to the numerical results, an expression regarding the focal distance variation is also derived for every combination of membrane radius R and membrane thickness t, for the considered material properties. This relationship is given by the following equation in which all quantities are represented in meters:

$$f = 2.789 \times 10^4 \, R^{\frac{2}{3}} \, t^{\frac{1}{3}} \tag{4.3}$$

For this situation, the maximum error regarding the focal distances obtained during the numerical simulations and as given by the present equation is 0.43%. Since the application of both equations (4.1) and (4.3) lead to marginal errors, their derivation proves to be an expedite tool for the conceptual design of such membrane-based parabolic collectors as a

function of its major geometrical features, namely its radius, thickness and focal distance. It should be noted however, that these expressions are only valid according to the material properties here considered for the Mylar® made membrane.

4.2.4 Light spot radius and light concentration capacity

The plot of Figure 43 illustrates the variation of the light spot radius localized at the focal plane as a function of the membrane radius for the four material thicknesses considered. It is possible to observe that as the radius of the circular membrane increases, the light spot radius in the focal plane tends to increase linearly, meaning then that the light dispersion becomes more critical for the situations of larger membranes with higher focal distances. Regarding the thickness, for a given membrane radius its variation is not considered to have a significant impact on the light spot radius size, even though this variation effectively may become slightly more pronounced as the radius of the circular membrane increases.

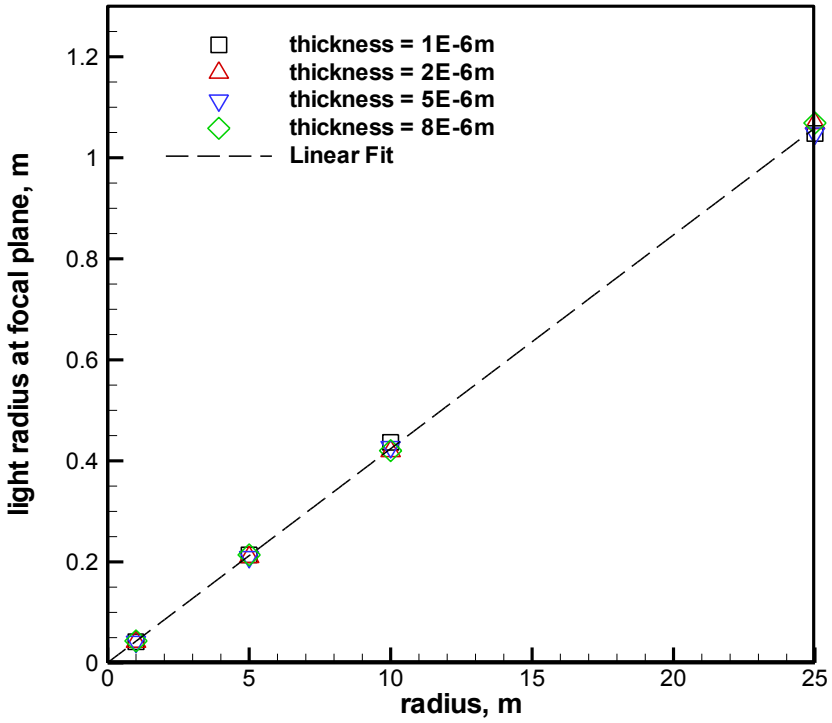

Figure 43 - Light spot radius variation with membrane radius *R* and thickness *t*.

In order to find an expression representative of light spot radius variation, a linear function is fitted to the corresponding data for every combination of membrane radius *R*. This relationship is given by following equation in which all quantities are represented in meters:

$$l = 0.0423R + 0.0007 \tag{4.4}$$

In the end, it is verified that the radius of the light spots in the focal plane are always about approximately 23 times less than the correspondent membrane radius values. Therefore, this means that such membrane-based type of structural configuration is capable of concentrating the incoming sunlight radiation more than an average of 550 times over the focal distance plane.

Chapter 5 – Boom-based parabolic solar collector

In the present chapter, the concept of a boom-based type of parabolic collector resembling an open umbrella is studied and analyzed. For this situation, the structure´s parabolic shape is guaranteed by the curvature provided by the rigidity of the booms, thus enabling its focal distance to be an initial known variable, as this becomes established during the design stage. In order to assess its structural response to the solar pressure load, namely to the impact on the resulting loadings and maximum deformations, a set of parametric studies are performed in ABAQUS® v6.11-3 taking into consideration the variation of several design features, such as the number of booms, number of supporting points of the membrane along the booms, structure´s size and membrane thickness. The effect due to an angular velocity around the structure´s symmetry axis as well as a different approach for the membranes geometry is also addressed. In the end, the mode shapes and respective natural frequencies of the structure are also determined in order to characterize its dynamic response under a linear regime.

5.1 Numerical model formulation

The numerical models considered during this case of study are composed of several parabolic--shaped circular cross-section booms manufactured in CFRP, a small tubular Aluminium mast in the middle, together with multiple doubly curved Mylar® made membrane gores, rigidly connected to the booms. All components are assigned isotropic material properties. Regarding the structure´s parabolic profile, it was stated that for the case of a parabolic solar sail application, the director´s position, which must correspond approximately to the focal distance, should coincide with about four times the stipulated collector´s radius value. Effectively, if the distance between these two components is too small, i.e. if a small focal distance is established, as the collector´s parabolic shape needs to become more exaggerated, this may result in a decrease of the effective sunlight collecting exposed area, thus reducing the amount of collected energy in order to propel the solar vehicle. On the other hand, if the focal distance is very high, this would imply for a very large connecting structure between the two components much harder to deploy in the space environment, as well as a more complex control system. Additionally, the whole structure would be more susceptible to undesired torques, therefore affecting its overall stability during a specific mission. For this research, independently of the considered structure´s size, the focal distance is always projected to be exactly four times the radius value, as this ratio proved to be satisfactory according to the previously mentioned reasons. Following this, both the booms and membranes geometric curvatures are sketched through several coordinate points which are obtained for a given radius with reference to equation 2.3.13. Concerning the section definition types, the mast and booms are modeled with B32 quadratic beam elements,

whereas for the membrane gores, M3D8 quadrilateral membrane elements are adopted as these proved to be the most reliable ones given the obtained results during the mesh study when compared for instance to the available shell types of elements. Once it is intended to assess the collector´s long term response due to the applied solar pressure over its membranes, a *Static General* type of analysis is again specified on the ABAQUS® Step module. This time however, since the membranes are provided with an initial curvature, they already have some degree of stiffness, which then allows for the simulations to be conducted with a good result precision through a linear approach, contrarily to the previous cases of study where geometric nonlinearity needed to be taken into consideration.

Although the collector´s symmetry axis is assumed to be perfectly aligned towards the incoming sunlight flux, since the structure presents an initial established parabolic curvature, this means that the resulting pressure magnitude inevitably decreases towards the outer edge surface elements as a result of its higher surface attitude angles. In order to take into account this variation, an expression based on equation 2.2.6 representative of its magnitude for a specific radius value, needs to be defined in the form of an *Analytical Field* in the ABAQUS® Load module. A spherical coordinate system also has to be created and correlated with the function for this purpose. Figure 44 shows an example of a 25m radius collector formed by six booms under solar pressure loading conditions.

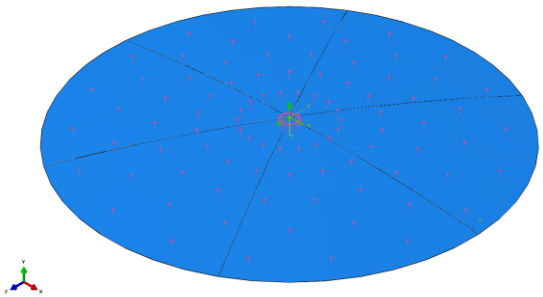

Figure 44 - Numerical model example under solar pressure loading conditions.

As the numerical model consists of a free flying structure in the space environment (unconstrained part), the ABAQUS® *Inertia Relief* feature is here specified as an additional loading condition rather than a common boundary condition. This technique allows balancing the externally applied solar pressure load with inertial loads induced from a constant rigid body acceleration field, i.e. by interpreting the mass of the model *Inertia Relief* submits this to a given acceleration in a way to counterbalance the applied external forces. Basically, an assumption is made that the structure is in a state of static equilibrium even though it is not constrained. When implementing this feature, a reference point in which an accelerating coordinate system needs to be specified, is attached to the structure´s centre of mass. In this case, it was chosen to be at the structure´s geometric centre and therefore coincident with origin´s coordinate system of the model.

5.2 Parametric studies

In this section, parametric studies are realized through a set of small adjustments on a numerical model of reference and the obtained results are analyzed and discussed. This baseline model, similar to the one presented in Figure 44, is formed by a total of six booms together with six membrane gores which are continuously connected to the booms across the edges. Its baseline dimensions as well as its material properties may be found in Table 5. With respect to the mast, its dimensions are always kept fixed regardless of the model considered.

Table 5 - Parabolic collector´s baseline dimensions and material properties.

Components:	**Booms**	**Mast**	**Membranes**
Radius [m]	0.12	0.08	N/A
Thickness [m]	$4.00E^{-4}$	0.005	$8.00E^{-6}$
Lenght [m]	25	2	25
Materials:	**CFRP**	**Aluminium**	**Mylar®**
Young Modulus [Gpa]	70	70	3.5
Poisson Ratio	0.1	0.32	0.38
Density [Kg/m^3]	1600	2700	1350

After a mesh convergence study has been performed on the baseline model, it was settled that a total of 102 B32 elements for the six booms and mast composition in conjunction with 650 M3D8 elements for each of six membrane gores, which are generated with a sweep mesh technique, would be refined enough to run the simulations accurately. Figures 45 and 46 illustrate the mesh attributes on both of these components.

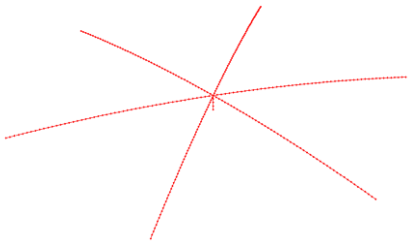

Figure 45 - Mast and booms mesh.

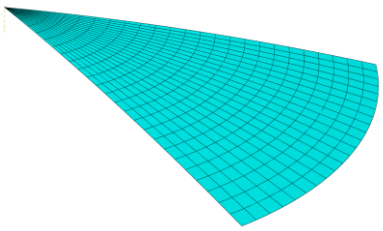

Figure 46 - Membrane gore sweep mesh.

5.2.1 Boom number

In this part, according to the baseline solar collector design, parametric studies are performed by changing the number of booms, while all the remaining properties and

dimensions are kept constant. In practise, a high number of booms would detrimentally compromise the structure´s final weight and most certainly its deployment effectiveness. On the other hand, if a low number of booms are implemented, even though the total membrane exposing area may be advantageously superior, as in this case each individual membrane gore film necessarily has to become larger and thus less stiff to bending, these may become more prone to instabilities, namely to the wrinkling phenomena, which would affect for instance the reflectivity of the solar photons into the director. The study of the wrinkling formation in the membranes is however beyond the scope of the present work. For this particular simulation, a total of six distinct models of increasing number of booms, varying from an initial value of four to a maximum of nine booms, are considered. The analysis show that the mass of the entire structure increases ranging from 83Kg for the four boom case to 143Kg for the nine boom case. The maximum boom tip deformations due to the solar pressure incidence over the membranes are shown in the plot of Figure 47 as a function of the number of booms adopted. Although the deformation magnitudes are very small, they also decrease rapidly with the increasing number of booms. Indeed, the maximum absolute deformation verified for instance to the six boom case is practically half the value verified on the four boom case.

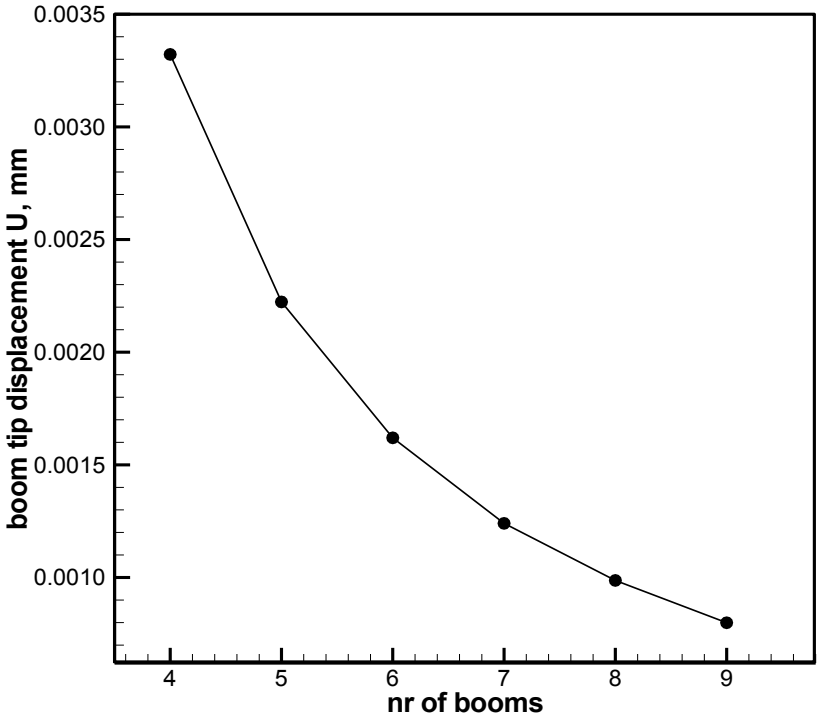

Figure 47 – Boom tip deflection with increasing number of booms.

Nevertheless, as expected the maximum deformations regarding the entire structure occur on the membrane components as a result of their lower inertia in relation to the booms. Regardless of the number of booms adopted, it is possible to observe that the deformation field over the membranes exhibits a wavy pattern across the structure's perimeter, being

that the maximum absolute deformation always manifests at a region next to the outer edges centre of each membrane gore. Figure 48 shows an arbitrary case concerning the deformation field of the baseline model.

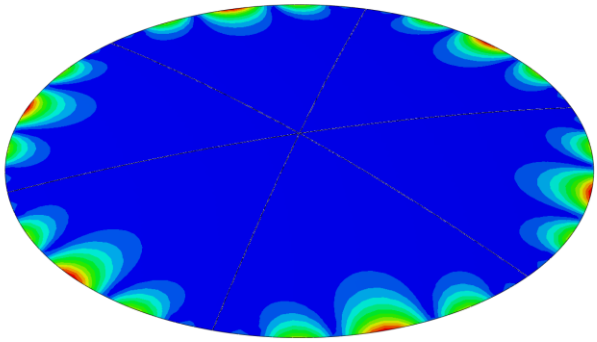

Figure 48 - Deformation field for the baseline collector case.

Regarding the membrane maximum deformation variation, a similar behaviour is verified in comparison to what is observed for the boom case enlighten in the plot of Figure 45. This time however, the deformation magnitudes verified on the membranes are approximately 100 times superior in relation to what is verified on the boom tips at each case.

After the deformation values have been discussed, the default Von Mises distortion energy criterion is used in order to perform the equivalent stress distribution analysis of the entire structure. Figures 49 and 50 are shown as two examples regarding the evolution of the equivalent stresses occurring between the five-boom and the eight-boom parabolic solar collector cases. Having in mind all of the models evolution, it is noticed that the maximum stress areas always tend to take place right next to the boom-membrane connections, namely on regions of about nearly two thirds of the radius value as well as on the model´s outer edge supporting points. Furthermore, as the number of booms is increased, the blue central bubble corresponding to the model´s lowest equivalent stress region is progressively enlarged as the stresses become more evenly distributed due to the superior number of booms.

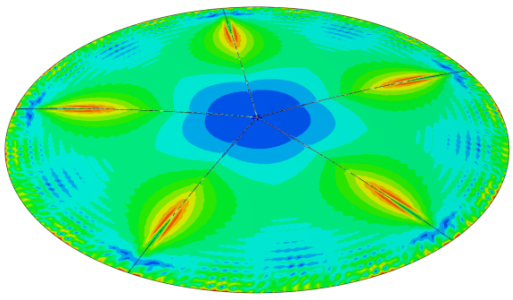

Figure 49 - Five-boom Von Mises stress distribution.

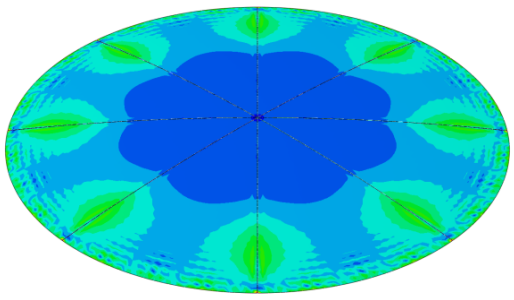

Figure 50 - Eight-boom Von Mises stress distribution.

5.2.2 Connecting points

For this situation, a parametric study which relies upon the consideration of four distinct cases of varying number of connecting points between the membrane gores and the booms is performed on the baseline model. Again, all the remaining properties and dimensions are kept constant. It should be noted that the connections here considered are defined as rigid connections through nodal *Tie* constraints on the ABAQUS® Interaction module. In practise however, these couplings would be most likely achieved through the adoption of some additional connecting elements, for instance with some sort of specific connecting cables, so this assumption should be viewed as a preliminary step for an investigation in this field.

The plot of Figure 51 gives both the boom tip and membrane maximum absolute deformations as a function of the four considered cases of increasing restraints. It is possible to notice that a drastic reduction of the resulting membrane deformations occurs when more than a total of five connecting points, i.e. when the membrane is attached to the booms by more than three points per edge, are defined. However, when nine connecting points are considered throughout the membrane´s edges, the resulting deformations prove to be very close to the case where continuously *Tie* constraints are established, so during the collector´s operation, it is possible to affirm that at least seventeen connections between these two elements should be taken into account for this given size. Independently of the considered number of supporting points, the maximum deformation regions are always localized at the same points, even though the deformation profiles do alter.

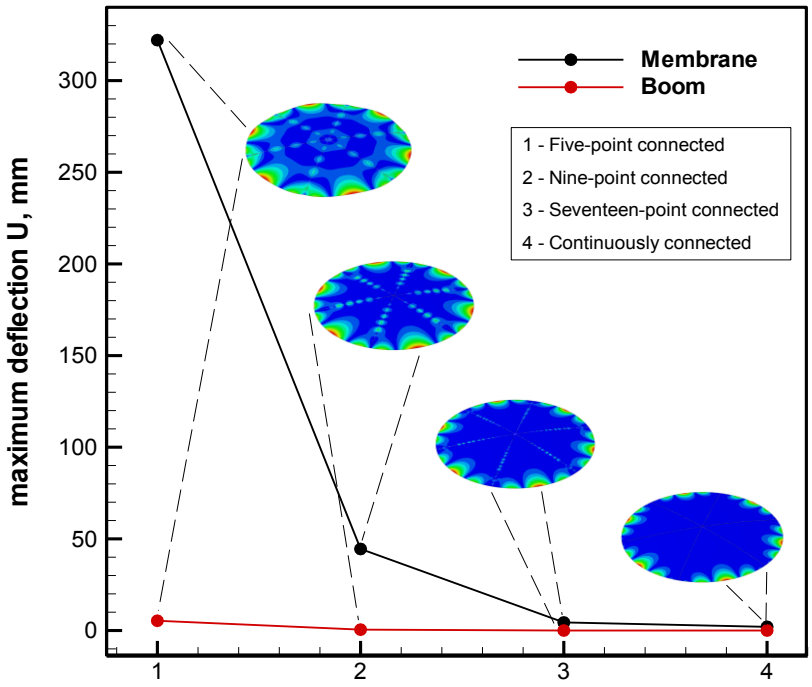

Figure 51 - Boom and membrane maximum deformations with increasing supporting points.

Figures 52 and 53 show two examples referring to the Von Mises stress distribution analysis of two of the previous models, in particular for the seventeen-point connected and the continuously connected solar collectors respectively. It becomes obvious that in comparison to the continuously connected model, for the seventeen-point connected case, a larger area associated with minimum stress fields covers the entire structure, as the higher tension regions tend to concentrate more near to the boom-membrane interfaces. Effectively, the maximum stress magnitudes computed for this situation shown to be practically nine times superior in relation to the ones verified on the continuously connected parabolic collector.

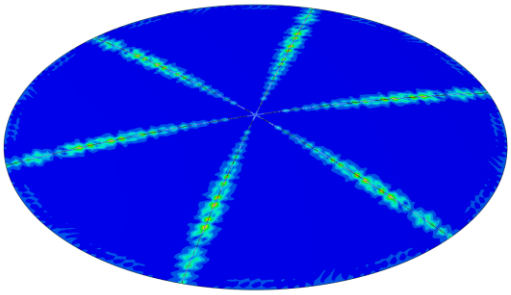

Figure 52 – Seventeen-point connected Von Mises stress distribution.

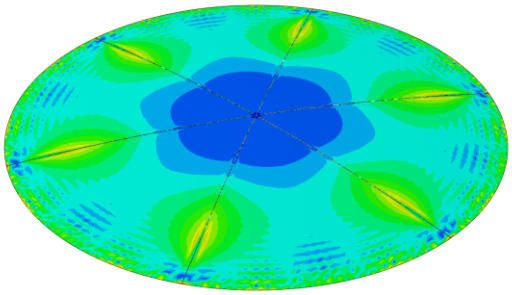

Figure 53 – Continuously connected Von Mises stress distribution.

Nevertheless, attending to Mylar's material datasheets [28], the maximum stress magnitude verified on the membranes for this particular case is found to be broadly apart from the material´s yielding stress values. In fact, even if the material´s yield strength when undergoing a very dramatic temperature scenario is to be considered, notably 13MPa for 200°C, the maximum stress due to solar pressure verified for seventeen-point connected parabolic collector membrane´s still represents merely 0.06% of the above mentioned value.

5.2.3 Solar collector size

During this section, a parametric study is conducted by altering the baseline model´s radius dimensions while maintaining all the other properties unaltered. The collector's designs considered during the analysis include eight discrete models of increasing radius size values, in particular 10, 14, 18, 25, 36, 50, 75 and 100m respectively. As the collector's size is increased, its total mass varies from 46Kg for the 10m radius case until 644Kg for the 100m radius case. The plot of Figure 54 describes the boom tip as well as the membrane maximum absolute deformations as a function of the collector´s radius size. It is possible to observe that as the radius size is increased, both the membrane and boom tip maximum deformations increase exhibiting a nonlinear growing behaviour trend as it would be expected. In this regard, the membranes for the 100m radius collector for instance, deform 220 times more than the ones of the 10m radius collector, although this is just one tenth of the size. For all

the models considered, the deformation field always resembles the same one as the baseline model presented in Figure 48.

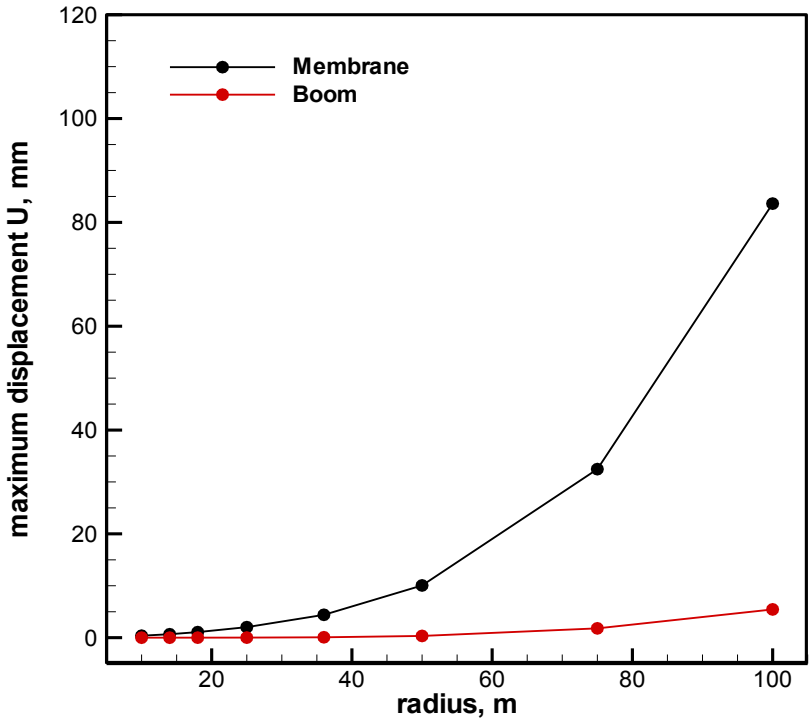

Figure 54 - Boom and membrane maximum deformations with increasing radius size.

5.2.4 Solar collector membrane thickness

For this case, a parametric study is conducted this time by changing the baseline model´s membrane thicknesses values while keeping the remaining properties unchanged. The collector's designs considered during this particular analysis also include eight distinct models of increasing membrane thickness values, in particular 1, 2, 3, 4, 5, 8, 13 and 20μm respectively. By increasing the membranes thickness, the parabolic collector´s overall mass ranged from 88Kg for the 1μm thickness case to 139Kg for the 20μm thickness case. The plot of Figure 55 describes the membrane maximum absolute deformation variation as a function of its thickness values. It should be noted that as the membrane thickness is increased, its maximum deformations decrease nonlinearly. This effect is most noticeable for the thinnest membranes, as the maximum deformations tend to converge into very small values afterwards. According to the obtained results, the solar collector´s thinnest membrane of 1μm has demonstrated to deform about 27 times more than the thickest one of 20μm. As it happened during the previous case of study, by changing the membrane thickness, the deformation patterns have demonstrated to remain unchanged in relation to what is verified for the baseline model case which can be visualized in Figure 48.

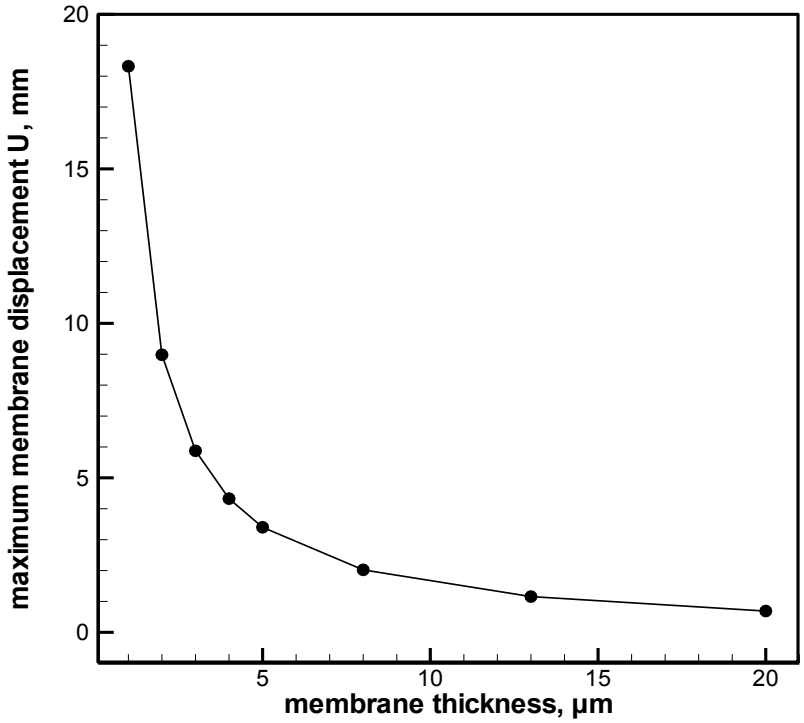

Figure 55 - Membrane maximum deformations with increasing thickness.

5.2.5 Angular velocity effect

For the following simulations, an additional loading condition is applied to baseline solar collector model, namely a rotary velocity around the structure´s symmetry axis and the resulting stresses and deformations under this regime are analyzed. In particular, it is demonstrated that by submitting the structure to very small angular velocity values, it is effectively possible to reduce at some extent the resulting deformations over the collector´s membranes. This may be explained as a result of the centrifugal forces induced due to the spacecraft's spinning motion which tend to pull the membranes radially outwards thus making them stiffer. Figure 56 gives an example of the resulting deformations for the collector under a given angular velocity.

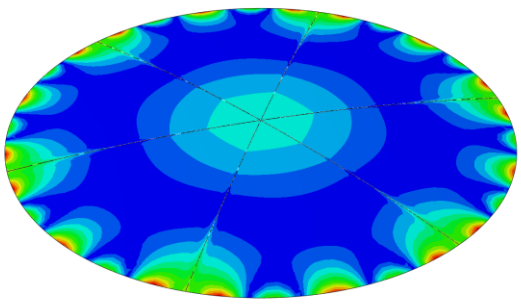

Figure 56 - Deformation field for collector under 0.044 rad/s angular velocity.

In this case, it is found that an angular velocity of 0.044 rad/s (0.42 RPM) represented the value capable of reducing to a minimum the maximum absolute deformations over the membranes as a result of the solar pressure load. Here, the maximum membrane absolute deformations turned out to be 17% the values where no angular velocity is taken into consideration. However, the booms showed to have a resulting deformation 14 times superior in relation to the baseline model, since as the collector begins to spin, its tips tend to deform upwards as a result of their higher inertia. In fact, under this condition, the boom tip deformations and membrane maximum deformation magnitudes actually become close to each other. Moreover, as it may be seen in Figure 56 the deformation field over the membranes also undergoes some modifications. Generally speaking, as the collector is submitted to some degree of angular velocity, in addition to central regions of each of the membrane gores outer edges, the maximum deformation areas also begin now to develop around the boom tip regions. Regarding the stress distribution, Figure 57 shows the Von Misses equivalent stresses over one of the membranes gores when undergoing this specific angular velocity value. As expected, the stress distribution assumes an increasing wavy pattern towards the outer edges. Here the maximum stress magnitude revealed to be approximately 2.4 times higher in comparison to the baseline model value.

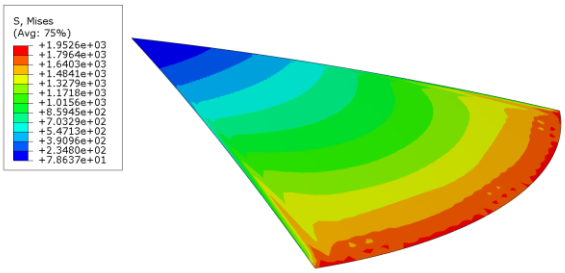

Figure 57 - Von Misses stresses over membrane gore under 0.044 rad/s angular velocity.

However, it was shown that by increasing the angular velocity a little more, namely to 0.049 rad/s (0.47 RPM), even though the maximum deformation magnitudes on the membranes are this time 20% the baseline model values, it is effectively possible to counteract its maximum deformation trend across the central outer edge regions, as it may be seen in Figure 58.

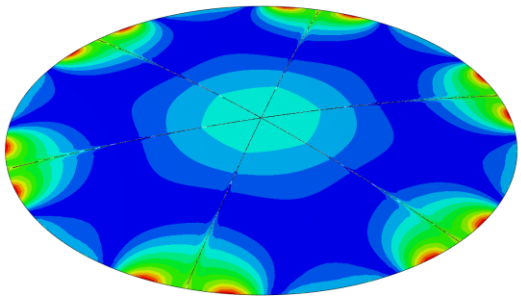

Figure 58 - Deformation field for collector under 0.049 rad/s angular velocity.

5.2.6 Membrane geometry

For this particular analysis, a different concept regarding the membrane gores geometry is also explored and the resulting deformations and stresses compared to the case of the baseline model. Specifically, the membrane´s outer curvilinear edges were suppressed, thus resembling now a doubly curved perfectly triangular shape. Figure 59 illustrates the resulting deformation field concerning this model. Even though it may be far similar to the baseline model case (Figure 48), it was proved that this new geometric approach could in fact reduce the membrane and boom tip deformations, as well as the stresses over the membrane gores.

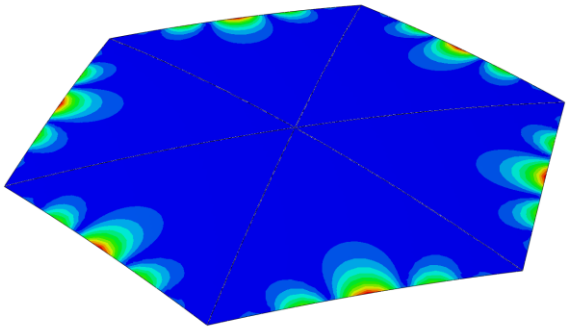

Figure 59 - Deformation field for the collector with new membrane approach.

More precisely, this new membrane concept enabled the collector to present a maximum membrane deformations of about 23% the values of the baseline model whereas for the boom tip deformations 43%. As for the membrane gore maximum stresses, whose distribution through the Von Misses criterion may be found in Figure 60, these have showed to be 38% the values verified for the baseline model.

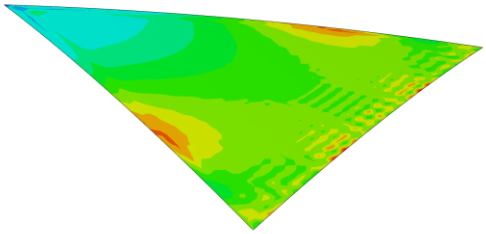

Figure 60 - Von Misses stresses over triangle-shaped membrane gore.

It should be noted however that despite the advantages concerning the minor resulting stresses and deformations, in practise this new geometric approach would have the drawback of presenting a lower sunlight exposing area, which would then compromise the maximization of the available thrust for the whole solar vehicle. According to this, the total membrane exposed area is in fact compromised almost one fifth in comparison to the area of the reference model.

5.3 Natural frequencies and mode shapes

In contrast to all of the previous analysis which are focused on the static response of the collector structure due to the applied solar pressure load over its membrane gores, in this section the mode shapes and respective natural frequencies of the parabolic collector are determined in order to characterize its dynamic response to loads in the linear equilibrium state. The modes of vibration inherent to these natural frequencies are of utmost importance since the deformation of the structure becomes maximal under these conditions, a phenomenon known as resonance. Therefore, it is always necessary to conceive a structure in such a way that the frequencies at which it may be submitted are not close to the natural frequencies at any circumstances. For the particular case of a solar sail, one should pay special attention to possible interference between the structure´s natural frequencies and for instance the frequencies induced by some sort of control system.

A new numerical model resembling the baseline model defined in section 5.2 was also conceived for this particular simulation. This time however, the tubular booms are modeled as shell shaped features instead, and the central mast to which these are rigidly connected, is replaced by a new central hexagonal hub shell part, as it can be demonstrated in Figure 61. The membrane gores are also suppressed, since its mass contribution is not considered to be meaningful on the collector´s overall mass, and hence not affecting in principle the natural frequency results. However, by keeping the boom radius and thicknesses constant, as it happens during the following simulations, this assumption only becomes valid if not very large structure sizes are to be adopted.

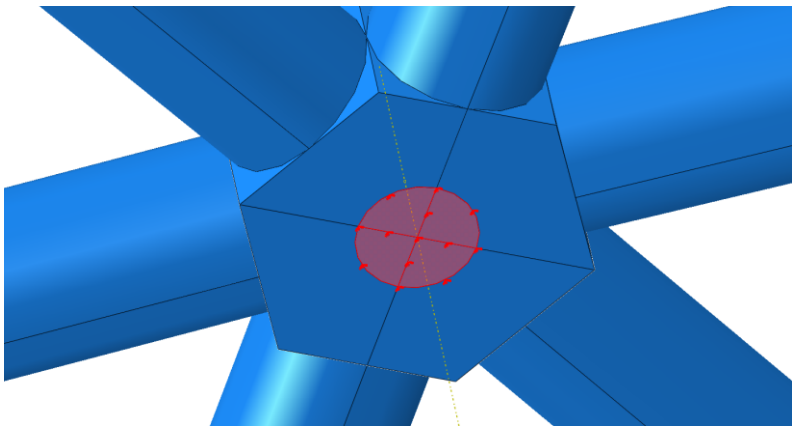

Figure 61 - Numerical model´s central hub with respective boundary condition.

The material elected is standard carbon fibre with epoxy resin. This time however, two different fibre stacking approaches for the booms will be considered during the analysis, namely with the fibres orientated at 0º/90º and 45º/-45º respectively. For this reason, when specifying the material properties on the ABAQUS® Property module, the *Lamina* type of

option has to be selected. In particular, these are attributed to the model according to a 0°/90° laminate orientation. Table 6 gives the corresponding properties. In order to specify the 45°/-45 ° fibre sequence to the section, a composite layup of a single 0.4 millimeter thickness ply needs to be defined with a rotation angle of 45°. By doing so half of the laminate fibres keep orientated at 45° while the remaining at -45° in relation to the booms longitudinal axis. If the rotation angle is kept at 0°, then the 0°/90° stacking is implemented.

Table 6 - Standard CFRP material properties for 0°/90° stacking [32].

Mechanical Properties of Carbon Fibre Composite / Epoxy with 0°/90° fibres	
Longitudinal Young Modulus E1 [GPa]	70
Transverse Young Modulus E2 [GPa]	70
In-plane Shear Young Modulus G12 [GPa]	5
Poisson Ratio	0.1
Density [Kg/m^3]	1600

Next, a *Frequency* type of analysis is specified on the ABAQUS® Step module. Here, the default *Lanczos* eigenvalue extraction method is defined and the first eight eigenvalues are requested to calculate the natural frequencies and the corresponding mode shapes of the system. In order to do so, ABAQUS® resorts to the *modal superposition* technique which is a very efficient method for linear problems of this nature.

Regarding the boundary conditions, since the *Inertia Relief* feature cannot be defined under a Frequency Step procedure, another solution needed to be found for this problem. Assuming that in practise the hub would probably be connected to some sort of a cylindrical component resembling a mast, a small circular partition is defined on the hub´s bottom base in order to simulate its interaction with the rest of the structure, or in other words, to create the model´s boundary condition. In this case, the circular partition is constrained across all degrees of freedom, except for the one translationally directed across the collectors normal axis (Figure 61). This hypothesis is translated as the most realistic one according to the expected behaviour of the structure in the space environment, even though a more elaborated future study should be performed on this subject.

During the analysis, each parabolic boom adopts a structured mesh technique defined with 16 elements across the circular perimeter and several elements across the length depending on the size considered. In the case of the 14m length boom for instance, shown in Figure 62, 11232 S4 elements are considered at each boom. For the case of the central hub, 794 S4 elements are always defined through a sweep generated approach regardless the size of the structure considered.

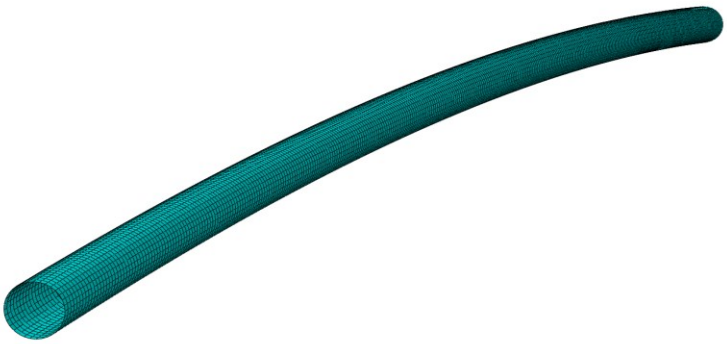

Figure 62 - Example of the mesh adopted for a 14 meter length parabolic boom.

The natural frequencies and respective mode shapes are computed for five different models of increasing boom length, including 10, 14, 18, 25 and 36m respectively. As it happened on the previous study, in this case the booms radius and thickness are also kept constant, as well as with the parabolic profile, whose focus is always projected to match exactly four times the considered radius value. Figure 63 shows an example concerning the 18m length boom model´s first eight vibration modes extracted from ABAQUS® through the previously described method. In this case, a 0°/90° stacking sequence is adopted.

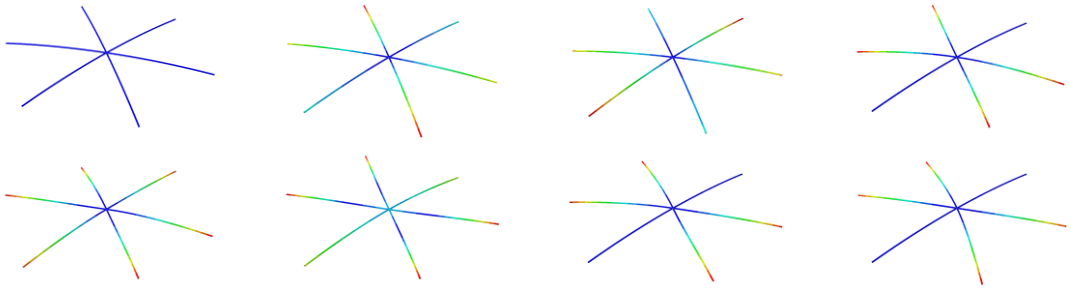

Figure 63 - Mode shapes for 18m collector booms with 0°/90° fibre sequence.

In the case of Figure 64, the same model undergoes the same procedure this time however with the 45°/-45 ° fibre approach.

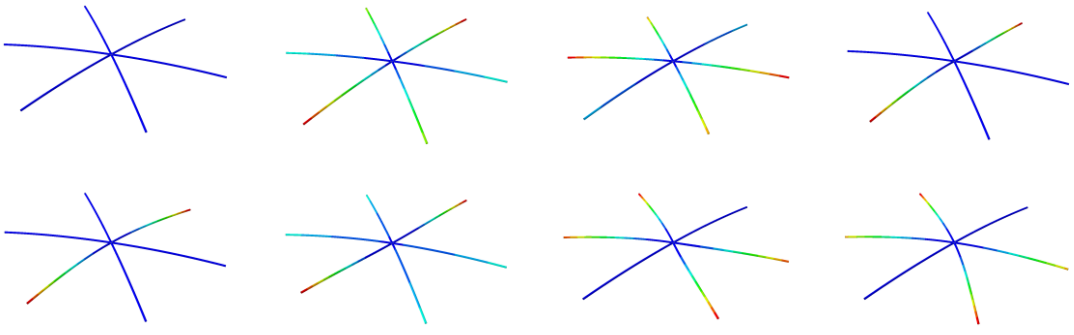

Figure 64 - Mode shapes for 18m collector booms with 45°/-45°fibre sequence.

The plot of Figure 65 shows four cases corresponding to the first eight natural frequencies variation in Hertz as a function of the booms length for both the 0°/90° and 45°/-45° fibre orientations. The first vibration frequency curves were omitted since its magnitudes are very close to zero, together with the third, fifth and seventh modes as its values proved to be closely spaced, from the preceding modes, particularly on the third and fifth mode, as well as from the following modes, as it was verified for the seventh mode. As expected, the results indicate that the considered frequency curves for each mode decreases, tending at the same time to become less separate as the boom length is increased. Moreover, the natural frequency magnitudes are always higher for the 0°/90 ° fibre orientations in comparison to the 45°/-45° as it can be seen for the fourth, sixth and eight modes. For the second mode this trend is almost negligible though. In the case of the 45°/-45° fibre orientation, all curves are also more closely spaced from each other.

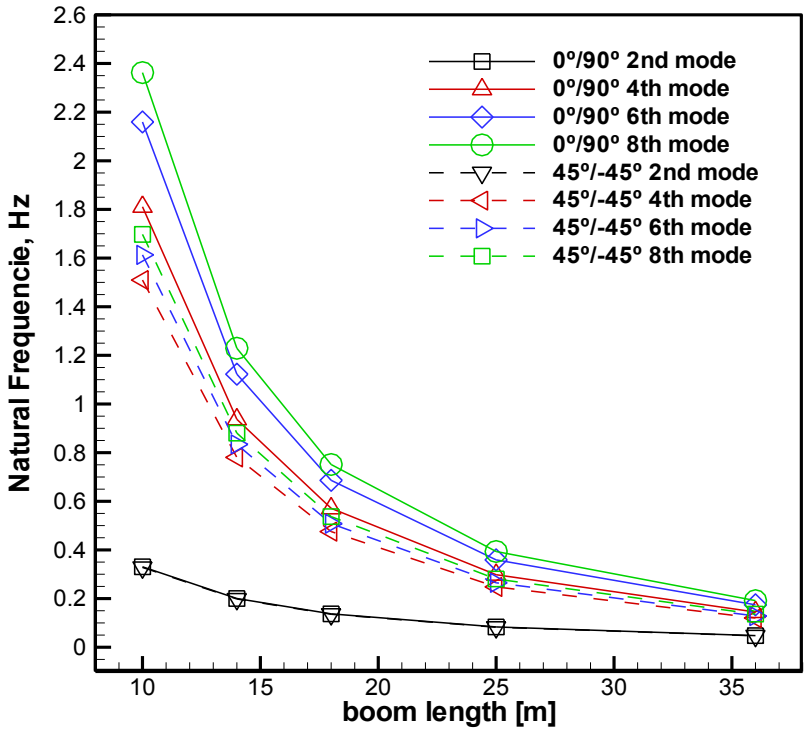

Figure 65 - Natural frequency variation as a function of boom length.

Chapter 6 – Conclusions and future work

6.1 Final conclusions

The present work allowed to assess the feasibility of several conceptual design possibilities for a parabolic space structure, intended primarily to operate as solar sail collector. In order to do so computational studies based on a set of numerical analysis were conducted by resorting to the finite element code ABAQUS® v6.11-3. According to these, some conclusions can be highlighted:

- Concerning membrane-like structural parts, if low thicknesses are considered, the maximum deformations under a uniform distributed pressure load have demonstrated to be quite similar regardless of the adopted element families and geometric orders. However, when initially flat membrane types of elements are implemented, a pre-tensioning strategy has to be necessarily defined to the model in order to obtain convergence. During the experimental tests, the obtained results concerning the three Mylar® samples slightly diverged from the numerical ones, which could be explained due to some level of uncertainty in the assignment of the correct material properties defined on the numerical model´s input. Nevertheless, an accurate representation of such membrane-based structural parts structural behaviour is effectively possible by defining these with isotropic material properties.

- Under the effect of solar pressure load, the resulting deformed shapes regarding the flat circular membrane, which prove to be very similar to parabolic ones, increase as the radius become larger and as the thickness decreases. As for the focal distances, these demonstrate to grow as the membrane radius is increased, and decrease with reducing thickness. However since these show to be very high as a result of the extremely low magnitude of the solar pressure, this structural concept does not become feasible for a solar sail collector application according to some of the reasons previously mentioned. Nevertheless, this may still prove to be very useful for space systems where focal distances would not need to be necessarily kept close to the collecting surface, such as for instance in solar-powered concentrators. In fact, this structural concept has demonstrated to be quite an effective power collector, as the membranes are capable of concentrating sunlight about 550 times over the focal plane.

- For the boom-based type of parabolic collector, the structure’s general response trends as a result of solar pressure incidence over the membrane gores have been

discussed. In particular, by altering several design parameters namely, the numbers of booms, number of supporting points, membrane thickness and structure´s size, the resulting deformation variations exhibit a nonlinear variation. The effects of a small angular velocity around the structure´s symmetry axis, as well as an alternative presented for the membrane gores geometries, proved to be capable of reducing to some extent the maximum deformations together with the whole displacement profile. Concerning the maximum stresses verified on the membrane gores, these proved to be insignificant since they are well below the material´s yielding stress. Lastly, the mode shapes and natural frequencies are determined for a structure composed by six booms with two different material fibre orientations in function of its size. The frequencies showed to decrease nonlinearly according to the increasing size of the structure, being that the 45°/-45° fibre stacking modes showed to be inferior in magnitude comparing to the 0°/90 ° composite orientation.

6.2 Prospects for future developments

Although the obtained results proved to be of great interest, the work here presented should be viewed as a preliminary step for an investigation concerning the structural behaviour of such solar-propelled spacecraft structures, inasmuch as it is based on several oversimplified assumptions regarding the proper definition of the numerical models. According to this, some crucial aspects that were here omitted are expected to be considered on the follow-up of the present study:

- Since in practise the membrane films are not capable of reflecting all the amount of incident light, its diffusion and absorption characteristics should be take into account, as these would lead to the achievement of more realistic results. This implicates an inferior force developed across the membrane surface, so the resulting deformations and focal distances verified on Chapter 4 for instance, must be seen as rather optimistic results.

- The membrane-based structural concept presented in Chapter 4 is assumed as being translationally constrained across its perimeter as some sort of “imaginary” boom in the shape of a ring was implemented in order to keep it in position. Since the boom is considered to be perfectly rigid, its inclusion on the numerical model is not expected to affect the membranes deformations. However, if this is provided with some degree elasticity, when loaded in compression, the membranes could in principle achieve higher deformations therefore allowing for lower focal distances to be obtained.

- Regarding the boom-based collector structure, a more realistic representation of the connections between the booms and membrane gores needs to be performed, as these in practise are not rigidly connected to each other, but most likely by some type of cable elements. The study of the wrinkling development in the membranes is also an issue of great importance that should be taken into account in a future stage.

References

[1]. Jerome L. Wright, "Space Sailing", *General Astronautics Corporation, Titsusville, Florida, USA*.

[2]. Colin R. McInnes, "Solar Sailing – Technology, Dynamics and Mission Applications"; Praxis Publishing, Chichester, UK, 1999.

[3]. Robert L. Forward, "Solar Photon Thrustor"; *Journal of Spacecraft and Rockets,* Vol. 27, No. 4, July-August 1990.

[4]. Guerman A. D., Smirnov, G. V., "Attitude dynamics of a compound solar sail". Proc. of the 57th International Astrodynamics Conference, Valencia, Spain, 2006, Paper IAC-06-C1.1.8.

[5]. Malcolm Macdonald, "*Solar Sailing: Applications and Technology Advancement*"; Advanced Space Concepts Laboratory University of Strathclyde, Glasgow, Scotland, E.U.

[6]. NASA Facts, "*Solar Sail Propulsion*", Pub 8-40377, April 2005. http://www.nasa.gov/centers/marshall/pdf/112341main_Solar_Sail_FS.pdf, last access: January 3, 2012.

[7]. Charles E. Garner, William Layman, Sarah A. Gavit, and Timothy Knowles, "*A Solar Sail Design for a Mission to the Near-Interstellar Medium*"; Jet Propulsion Laboratory, California Institute of Technology, Pasadena, Ca 91109.

[8]. Giovanni Vulpetti, Les Johnson and Gregory L. Matloff, "Solar Sails – A novel approach to interplanetary travel"; Praxis Publishing Ltd 2008.

[9]. M. Vasil, "*The Suaineadh Project: A stepping stone towards the deployment of large flexible structures in space*"; Space Advanced Research Team, University of Glasgow, United Kingdom.

[10]. L. Herbeck, M. Eiden, M. Leipold, C. Sickinger, W. Unckenbold,*"Development and Test of Deployable Ultra-Lightweight CFRP Booms for a Solar Sail"*; Institute of Structural Mechanics, German Aerospace Center (DLR), Lilienthalplatz 7, D-38108 Brunswick, Germany.

[11]. M. Leipold, H. Runge, C. Sickinger, "*Large SAR Membrane antennas with lightweight deployable booms*"; Institute of Structural Mechanics, German Aerospace Center (DLR), Lilienthalplatz 7, D-38108 Brunswick, Germany.

[12]. Corona-resistant (CR) Polyimide Film /Kapton Film; Tianjin Heng Tong Era Electrical Material Technology Co., Ltd. http://tjhengtong.en.alibaba.com/product/306463288-210291753/Corona resistant CR Polyimide Film Kapton Film.html, last access: January 7, 2012.

[13]. Mylar 60 Film Spec Sheet; Conklin Metal Industries. http://www.conklinmetal.com/files/Images/mylar-A_11_6_2008_8_58_56_PM.jpg, last access: January 8, 2012.

[14]. Hiroshi Furuya, Osamu Mori, Hirotaka Sawada, Nobukatsu Okuizumi, Yoji Shirasawa, M.C. Natori, Yasuyuki Miyazaki and Saburo Matunaga, "Manufacturing and Folding of Solar Sail "IKAROS"; 52nd AIAA/ASME/ASCE/AHS/ASC Structures, Structural Dynamics and Materials Conference
 19th 4 - 7 April 2011, Denver, Colorado.

[15]. Nobukatsu Okuizumi, Azusa Mura, Saburo Matsunaga, Hiraku Sakamoto, Yoji Shirasawa and Osamu Mori, "Small-scale Experiments and Simulations of Centrifugal Membrane Deployment of Solar Sail Craft "IKAROS"; 52nd AIAA/ASME/ASCE/AHS/ASC Structures, Structural Dynamics and Materials Conference
 19th 4 - 7 April 2011, Denver, Colorado.

[16]. Yuichi Tsuda, Takanao Saiki, Ryu Funase, Yoji Shirasawa and Yuya Mimasu, "Shape Parameters Estimation of IKAROS Solar Sail Using In-Flight Attitude Determination Data; AIAA/ASME/ASCE/AHS/ASC Structures, Structural Dynamics and Materials Conference
 19th 4 - 7 April 2011, Denver, Colorado.

[17]. David W. Sleight and Danniella M. Muheim, "Parametric Studies of Square Solar Sails Using Finite Element Analysis"; NASA Langley Research Center, Hampton, VA 23681-2199, U.S.A.

[18]. Zheng Jinjin, Sheng Zhaoyu, Zhou Hongjun, Huang Wenhao and Sheng Lianguan, "Structural analysis about a new solar sail"; *Chin. J. Space Sci.*, 2009, 29(2): 249~256.

[19]. Barmac K. Taleghani, Peter S. Lively, James L. Gaspar, David M. Murphy and Thomas A. Trautt, "Dynamic and static shape test/analysis correlation of a 10 meter quadrant solar sail"; *NASA Langley, Army Research Laboratory* / Lockheed Martin Space

Operations / *NASA Langley Research Center, Hampton, VA / ATK Space Systems, Goleta, CA.*

[20]. Y.W. Wong and S. Pellegrino, "Wrinkles in Square Membranes"; SKM Consultants (M) Sdn Bhd, Suite E-15-01, Plaza Mont' Kiara, No. 2, Jalan Kiara, Mont' Kiara, 50480 Kuala Lumpur, MALAYSIA / Department of Engineering, University of Cambridge, Trumpington Street, Cambridge, CB2 1PZ, U.K.

[21]. Alexander Tessler and David W. Sleight, "Toward Effective Shell Modeling of Wrinkled Thin-Film Membranes Exhibiting Stress Concentrations"; Analytical and Computational Methods Branch, M/S 240, Structures and Materials Competency, NASA Langley Research Center, Hampton, VA 23681-2199, U.S.A.

[22]. S. Pellegrino, "CRTS Reflectors"; *Department of Engineering, University of Cambridge Trumpington Street, Cambridge, CB2 1PZ, U.K.*

[23]. D. K. Marker and C. H. Jenkins, "Surface precision of optical membranes with curvature"; Advanced Optics and Imaging Division, Air Force Research Laboratory 3550 Aberdeen Ave SE / Mechanical Engineering Dept. SD School of Mines and Technology, Rapid City, SD 57701.

[24]. Yan Xu and Fu-ling Guan, "Structure design and mechanical measurement of inflatable antenna"; Acta Astronautica 76 (2012) 13-25.

[25]. Tham Sreekantamurthy, James L. Gaspar, Troy Mann, Vaughn Behun, James C. Pearson, Stephen Scarborough; *"Nonlinear Structural Analysis Methodology and Dynamics Scaling of Inflatable Parabolic Reflector Antenna Concepts"*; 48th AIAA/ASME/ASCE/AHS/ASC Structures, Structural Dynamics, and Materials Conference, Waikiki, Haway; United States; 23-27 April 2007.

[26]. NASA, May 1998, "Deflection of Circular Membrane under Differential Pressure", Report No. GSC-13783, NASA Tech Briefs; http://www.techbriefs.com/index.php?option=com_staticxt&staticfile=/Briefs/Sept99/GSC14223.html, last access: March 20, 2012.

[27]. *Abaqus 6.11 Verification Manual*. http://abaqus.ethz.ch:2080/v6.11/books/ver/default.htm, last access: September 4, 2012.

[28]. Typical Physical and Thermal Properties of Mylar® Polyester Film;

http://usa.dupontteijinfilms.com/informationcenter/downloads/Physical_And_Thermal_Properties.pdf, last access: February 8, 2012.

[29]. DuPont™ Teijin Mylar® Polyester Films; http://www.matweb.com/search/MaterialGroupSearch.aspx, last access: February 7, 2012.

[30]. Benjamin Schneuwly, "Some studies about FEM simulation of membranes for a parabolic solar sail", IAESTE Internship, Aeronautics and Astronautics Research Center University of Beira Interior, December 2011.

[31]. Understanding Nonlinear Analysis – Solid Works. http://files.solidworks.com/whitepapers/2010/Nonlinear_Analysis_2010_ENG_FINAL.pdf, last access: July 5, 2012.

[32]. Mechanical Properties of Carbon Fibre Composite Materials, Fibre / Epoxy Resin; http://www.performance-composites.com/carbonfibre/mechanicalproperties_2.asp, last access: September 28, 2012.

Annex A - MATHEMATICA® analytical theorem for circular membrane

$w = \text{w0} * (1 - (r/R)\text{^}2)$

$(1 - \frac{r^2}{R^2})\text{w0}$

$u = r * (R - r) * (\text{C1} + \text{C2} * r)$

$r(\text{C1} + \text{C2}r)(-r + R)$

$\text{dudr} = D[u, \{r, 1\}]$

$-r(\text{C1} + \text{C2}r) + \text{C2}r(-r + R) + (\text{C1} + \text{C2}r)(-r + R)$

$\text{dwdr} = D[w, \{r, 1\}]$

$-\frac{2r\text{w0}}{R^2}$

$\text{er} = \text{dudr} + (1/2) * \text{dwdr}\text{^}2$

$-r(\text{C1} + \text{C2}r) + \text{C2}r(-r + R) + (\text{C1} + \text{C2}r)(-r + R) + \frac{2r^2\text{w0}^2}{R^4}$

Simplify[er]

$\text{C1}(-2r + R) + r(-3\text{C2}r + 2\text{C2}R + \frac{2r\text{w0}^2}{R^4})$

$\text{et} = u/r$

$(\text{C1} + \text{C2}r)(-r + R)$

$\text{IntegralArgument} = (\text{er}\text{^}2 + \text{et}\text{^}2 + 2 * \text{niu} * \text{er} * \text{et}) * r$

$r((\text{C1} + \text{C2}r)^2(-r + R)^2 + 2\text{niu}(\text{C1} + \text{C2}r)(-r + R)(-r(\text{C1} + \text{C2}r) + \text{C2}r(-r + R) + (\text{C1} + \text{C2}r)(-r + R) + \frac{2r^2\text{w0}^2}{R^4}) + (-r(\text{C1} + \text{C2}r) + \text{C2}r(-r + R) + (\text{C1} + \text{C2}r)(-r + R) + \frac{2r^2\text{w0}^2}{R^4})^2)$

Simplify[IntegralArgument]

$r((\text{C1} + \text{C2}r)^2(r - R)^2 + \frac{2\text{niu}(\text{C1} + \text{C2}r)(r - R)(\text{C1}(2r - R)R^4 + r(\text{C2}(3r - 2R)R^4 - 2r\text{w0}^2))}{R^4} + \frac{(\text{C1}R^4(-2r + R) + r(\text{C2}R^4(-3r + 2R) + 2r\text{w0}^2))^2}{R^8})$

$\text{SolvedIntegral} = \text{Integrate}[\text{IntegralArgument}, \{r, 0, R\}]$

$\frac{\text{C1}^2R^4}{4} + \frac{3}{10}\text{C1C2}R^5 + \frac{7\text{C2}^2R^6}{60} - \frac{3}{5}\text{C1}R\text{w0}^2 + \frac{1}{5}\text{C1niu}R\text{w0}^2 - \frac{2}{5}\text{C2}R^2\text{w0}^2 + \frac{2}{15}\text{C2niu}R^2\text{w0}^2 + \frac{2\text{w0}^4}{3R^2}$

$U = (\text{pi} * \text{EModulus} * t/(1 - \text{niu}\text{^}2)) * (\text{SolvedIntegral})$

$\frac{\text{EModuluspi}t(\frac{\text{C1}^2R^4}{4} + \frac{3}{10}\text{C1C2}R^5 + \frac{7\text{C2}^2R^6}{60} - \frac{3}{5}\text{C1}R\text{w0}^2 + \frac{1}{5}\text{C1niu}R\text{w0}^2 - \frac{2}{5}\text{C2}R^2\text{w0}^2 + \frac{2}{15}\text{C2niu}R^2\text{w0}^2 + \frac{2\text{w0}^4}{3R^2})}{1 - \text{niu}^2}$

Simplify[U]

$-\frac{\text{EModuluspi}t(15\text{C1}^2R^6 + 7\text{C2}^2R^8 + 8\text{C2}(-3 + \text{niu})R^4\text{w0}^2 + 40\text{w0}^4 + 6\text{C1}R^3(3\text{C2}R^4 + 2(-3 + \text{niu})\text{w0}^2))}{60(-1 + \text{niu}^2)R^2}$

dUdC1 = $D[U,\{C1,1\}]$

$$\frac{\text{EModuluspi}t\left(\frac{C1R^4}{2}+\frac{3C2R^5}{10}-\frac{3R\text{w}0^2}{5}+\frac{1}{5}\text{niu}R\text{w}0^2\right)}{1-\text{niu}^2}$$

dUdC2 = $D[U,\{C2,1\}]$

$$\frac{\text{EModuluspi}t\left(\frac{3C1R^5}{10}+\frac{7C2R^6}{30}-\frac{2R^2\text{w}0^2}{5}+\frac{2}{15}\text{niu}R^2\text{w}0^2\right)}{1-\text{niu}^2}$$

Solve[{dUdC1 == 0, dUdC2 == 0}, {C1, C2}]

$$\left\{\left\{C1\to-\frac{-3\text{w}0^2+\text{niuw}0^2}{4R^3},\ C2\to-\frac{-3\text{w}0^2+\text{niuw}0^2}{4R^4}\right\}\right\}$$

$$\begin{aligned}\text{Unew} = -\frac{1}{60(-1+\text{niu}^2)R^2}\text{EModuluspi}t\Big(&15\left(-\frac{-3\text{w}0^2+\text{niuw}0^2}{4R^3}\right)^2R^6+7\left(-\frac{-3\text{w}0^2+\text{niuw}0^2}{4R^4}\right)^2R^8\\&+8\left(-\frac{-3\text{w}0^2+\text{niuw}0^2}{4R^4}\right)(-3+\text{niu})R^4\text{w}0^2+40\text{w}0^4\\&+6\left(-\frac{-3\text{w}0^2+\text{niuw}0^2}{4R^3}\right)R^3\left(3\left(-\frac{-3\text{w}0^2+\text{niuw}0^2}{4R^4}\right)R^4+2(-3+\text{niu})\text{w}0^2\right)\Big)\end{aligned}$$

$$-\frac{\text{EModuluspi}t\left(40\text{w}0^4-2(-3+\text{niu})\text{w}0^2\left(-3\text{w}0^2+\text{niuw}0^2\right)+\frac{11}{8}\left(-3\text{w}0^2+\text{niuw}0^2\right)^2-\frac{3}{2}\left(-3\text{w}0^2+\text{niuw}0^2\right)\left(2(-3+\text{niu})\text{w}0^2-\frac{3}{4}\left(-3\text{w}0^2+\text{niuw}0^2\right)\right)\right)}{60(-1+\text{niu}^2)R^2}$$

Simplify[Unew]

$$\frac{\text{EModulus}(-7+\text{niu})\text{pi}t\text{w}0^4}{24(-1+\text{niu})R^2}$$

IntegralArgument2 = $(w*P*r)$

$$Pr\left(1-\frac{r^2}{R^2}\right)\text{w}0$$

SolvedIntegral2 = Integrate[IntegralArgument2, $\{r,0,R\}$]

$$\frac{1}{4}PR^2\text{w}0$$

W = (2 * pi * (SolvedIntegral2))

$$\frac{1}{2}P\text{pi}R^2\text{w}0$$

PotentialEnergy = Unew + W

$$\frac{1}{2}P\text{pi}R^2\text{w}0-\frac{\text{EModuluspi}t\left(40\text{w}0^4-2(-3+\text{niu})\text{w}0^2\left(-3\text{w}0^2+\text{niuw}0^2\right)+\frac{11}{8}\left(-3\text{w}0^2+\text{niuw}0^2\right)^2-\frac{3}{2}\left(-3\text{w}0^2+\text{niuw}0^2\right)\left(2(-3+\text{niu})\text{w}0^2-\frac{3}{4}\left(-3\text{w}0^2+\text{niuw}0^2\right)\right)\right)}{60(-1+\text{niu}^2)R^2}$$

Simplify[PotentialEnergy]

$$\frac{\text{piw}0\left(12(-1+\text{niu})PR^4+\text{EModulus}(-7+\text{niu})t\text{w}0^3\right)}{24(-1+\text{niu})R^2}$$

dPotentialEnergydw0 = D[PotentialEnergy, {w0,1}]

$$\begin{aligned}\frac{1}{2}P\text{pi}R^2-\frac{1}{60(-1+\text{niu}^2)R^2}\text{EModuluspi}t\Big(&160\text{w}0^3-2(-3+\text{niu})\text{w}0^2(-6\text{w}0+2\text{niuw}0)-4(-3\\&+\text{niu})\text{w}0\left(-3\text{w}0^2+\text{niuw}0^2\right)+\frac{11}{4}(-6\text{w}0+2\text{niuw}0)\left(-3\text{w}0^2+\text{niuw}0^2\right)-\frac{3}{2}(-3\text{w}0^2\\&+\text{niuw}0^2)\left(4(-3+\text{niu})\text{w}0-\frac{3}{4}(-6\text{w}0+2\text{niuw}0)\right)-\frac{3}{2}(-6\text{w}0+2\text{niuw}0)\left(2(-3+\text{niu})\text{w}0^2\right.\\&\left.-\frac{3}{4}\left(-3\text{w}0^2+\text{niuw}0^2\right)\right)\Big)\end{aligned}$$

Solve[{dPotentialEnergydw0 == 0}, {w0}]

$$\{\{w0 \to -\frac{(-3)^{1/3}P^{1/3}R^{2/3}}{(-\frac{7EModulust}{(1-niu^2)R^2}-\frac{6EModulusniut}{(1-niu^2)R^2}+\frac{EModulusniu^2t}{(1-niu^2)R^2})^{1/3}}\},\{w0 \to \frac{3^{1/3}P^{1/3}R^{2/3}}{(-\frac{7EModulust}{(1-niu^2)R^2}-\frac{6EModulusniut}{(1-niu^2)R^2}+\frac{EModulusniu^2t}{(1-niu^2)R^2})^{1/3}}\},\{w0 \to \frac{(-1)^{2/3}3^{1/3}P^{1/3}R^{2/3}}{(-\frac{7EModulust}{(1-niu^2)R^2}-\frac{6EModulusniut}{(1-niu^2)R^2}+\frac{EModulusniu^2t}{(1-niu^2)R^2})^{1/3}}\}\}$$

Simplify[$\frac{3^{1/3}P^{1/3}R^{2/3}}{(-\frac{7EModulust}{(1-niu^2)R^2}-\frac{6EModulusniut}{(1-niu^2)R^2}+\frac{EModulusniu^2t}{(1-niu^2)R^2})^{1/3}}$]

$$\frac{3^{1/3}P^{1/3}R^{2/3}}{(-\frac{EModulus(-7+niu)t}{(-1+niu)R^2})^{1/3}}$$

$f = (R\text{^}2)\Big/(4 * \frac{3^{1/3}P^{1/3}R^{2/3}}{(-\frac{EModulus(-7+niu)t}{(-1+niu)R^2})^{1/3}})$

$$\frac{R^{4/3}(-\frac{EModulus(-7+niu)t}{(-1+niu)R^2})^{1/3}}{43^{1/3}P^{1/3}}$$

Annex B – Mylar® samples mid-point displacement plots

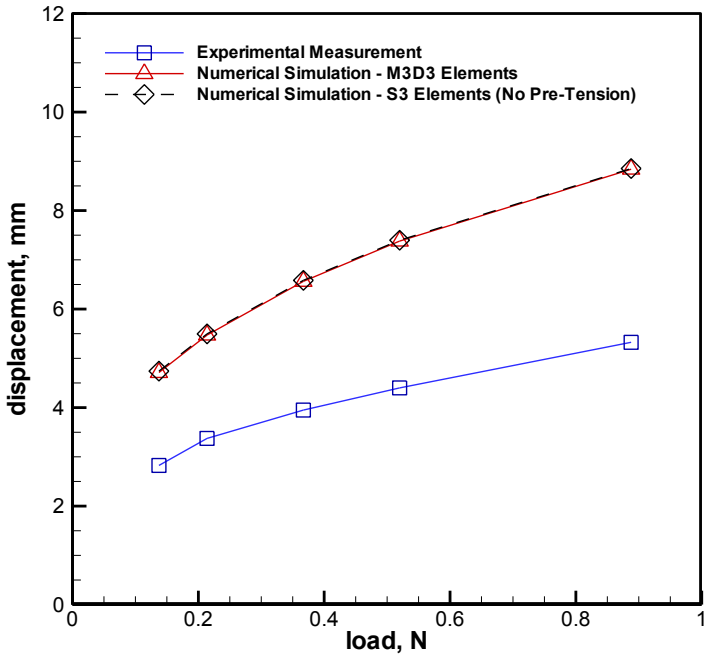

Figure B.1 - Experimental and numerical results of mid-point displacements verified for Non-specified type of Mylar® of 5μm film.

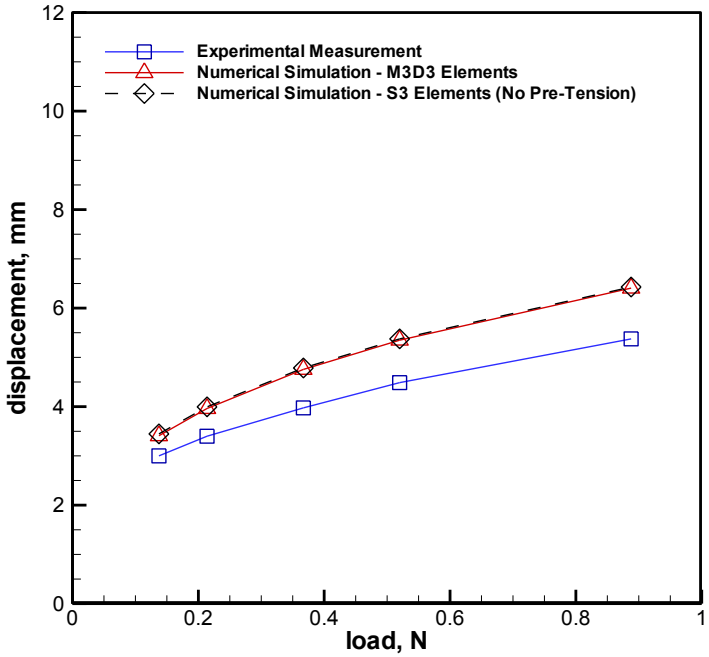

Figure B.2 - Experimental and numerical results of mid-point displacements verified for Mylar® OL 140L of 13μm film.

Annex C - MATLAB® solar pressure iterative calculation code

```
clear
clc
clf
close  all
clear  al
format long

tic             % Timer

% Definition of Variables

rad=1;          % Radius of the Circular Membrane [m]
P0=9.12e-6;     % Solar Pressure [Pa]
stop=1e-6;      % Maximum Tolerated Relative Error / Criterion to abort the
                  iterative calculation
nr=16;          % Number of nodes in Radius direction (including middle one)
nt=931;         % Total number of nodes
ne=930;         % Total number of elements



% Create and delete .txt files

fid = fopen('data.txt', 'w');
      fclose(fid);

      h=1/(nr-1)

fid = fopen('data.txt', 'a+');
      for i=0:nr-1
      fprintf(fid,'%8.4f,\t0,\t0, \n',h*i)
      end
      fclose(fid);

fid = fopen('step.txt', 'w');
      fclose(fid);


% Definition of Parameters

nc=(nt-1)/(nr-1);   % Number of Radials
error=10000;        % Error Values
k=1;
y=[]


% Program to calculate circular membrane deflection with non-uniform P0

while error > stop
    data=load(['data.txt']);
    oldy=y;
    y=data(1:nr,3)
    x=[];

    for i=1:nr
    x=[x;sqrt(data(i,1)^2)]    % Make x coordinates positive for plotting
    end


   % Relative Error
```

```
   if k>2
        sum=0;
        sum1=0;

        for i=1:nr-1
            sum=sum1+sqrt((y(i)/oldy(i)-1)^2)
            sum1=sum;
        end

        error=sum1/(nr-1);

        end


% Interpolation with Polyfit Function

% Degree of polynomial approaching the membrane deflection
  n=6;

intpol = polyfit(x,y,n)

% Coefficients for the derivative of the membrane deflection function
a1=intpol(1)*6
b1=intpol(2)*5
c1=intpol(3)*4
d1=intpol(4)*3
e1=intpol(5)*2
f1=intpol(6)*1

% Slope of the resulting membrane deflection for given x coordinates
  dzdy=polyval([a1 b1 c1 d1 e1 f1],x)

% Angle of the resulting membrane deflection for given x coordinate
  angle=atan(dzdy);

% Factor from which P0 is multiplied
  f=cos(angle).^2;


% Print new step top to "step.txt" file
  fid = fopen('step.txt', 'w+');
   fprintf(fid,'*Step, name=Step-1, nlgeom=YES, inc=500\n*Static\n1e-25, 1.,
    1e-50, 1.\n*Boundary\n_PickedSet4, 1, 1\n_PickedSet4, 2, 2\n_PickedSet4,
    3, 3\n*Dload\n');


% Pressure for all the membrane elements except central ones
  for i=1:ne-nc
     fprintf(fid,'Part-1-1.%i, P, %16.12f \n',i,P0*(f(mod(i-1,nr-
     2)+2)+f(mod(i-1,nr-2)+3))/2);
     end

% Pressure for elements around the central node
   for i=ne+1-nc:ne
     fprintf(fid,'Part-1-1.%i, P, %16.12f \n',i,(P0*(f(1)+f(2))/2));
     end

   fprintf(fid,'*Output, field\n*Node Output\nCOORD\n*End
   Step\n**********************************************************\n');
    fclose(fid);



if error < stop
   break
     end
```

```
   k
   k=k+1;


% Plotting of resulting membrane deflection polynomial function

intpol=plot(x,y,'-bs', 'LineWidth', 1);
title('Membrane Deformed Shape');
xlabel('radius [m]')
ylabel('displacement [m]')
hold on


% ABAQUS job and python script execution commands

 !abaqus job=circular interactive
 !abaqus python output.py

pause(5)

end


% Indication that job is completed without errors
  fprintf(':-)...Calculation Completed...:-)')

toc


% Play sound when job is completed

cf = 2000;                  % carrier frequency (Hz)
sf = 22050;                 % sample frequency (Hz)
d = 1.5;                    % duration (s)
n = sf * d;                 % number of samples
s = (1:n) / sf;             % sound data preparation
s = sin(2 * pi * cf * s);   % sinusoidal modulation
sound(s, sf);               % sound presentation
pause(d + 0.5);             % waiting for sound end
```

Annex D - Non-dimensional displacements for varying membrane thickness

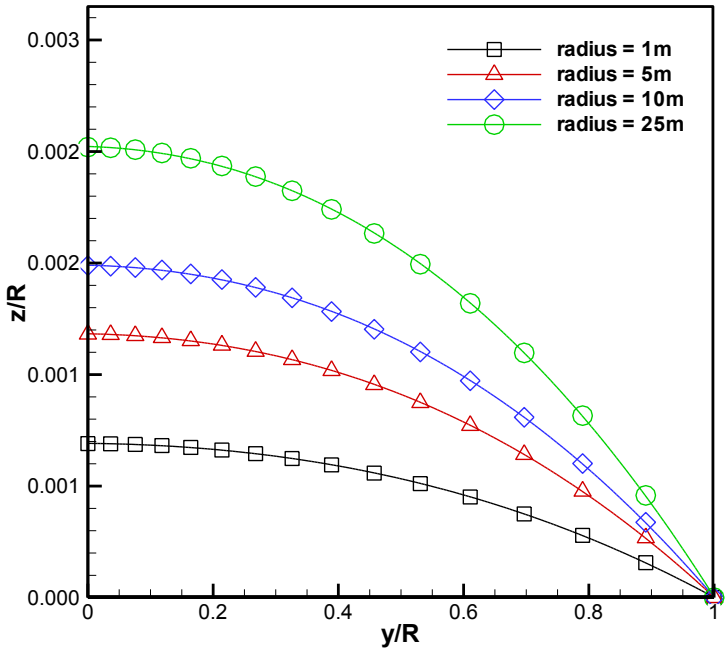

Figure D.1 - Non-dimensional displacement variation for the 2µm thickness membranes.

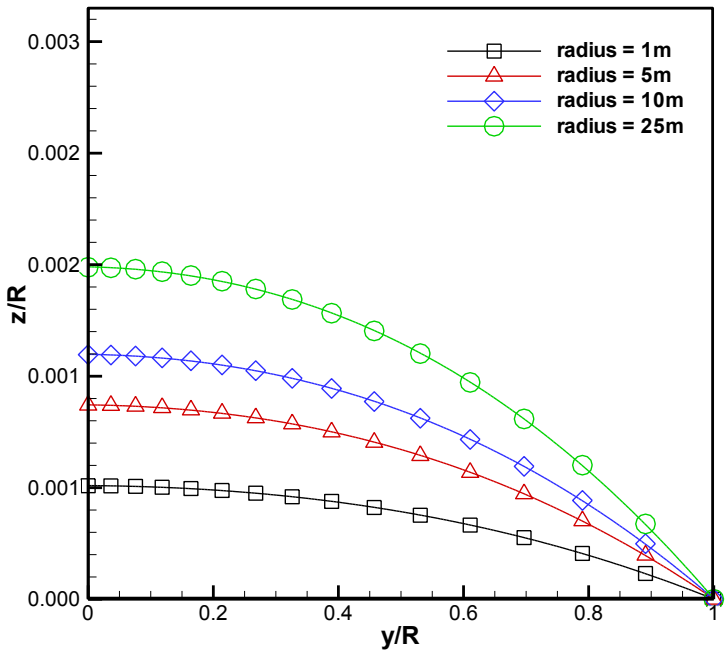

Figure D.2 - Non-dimensional displacement variation for the 5µm thickness membranes.

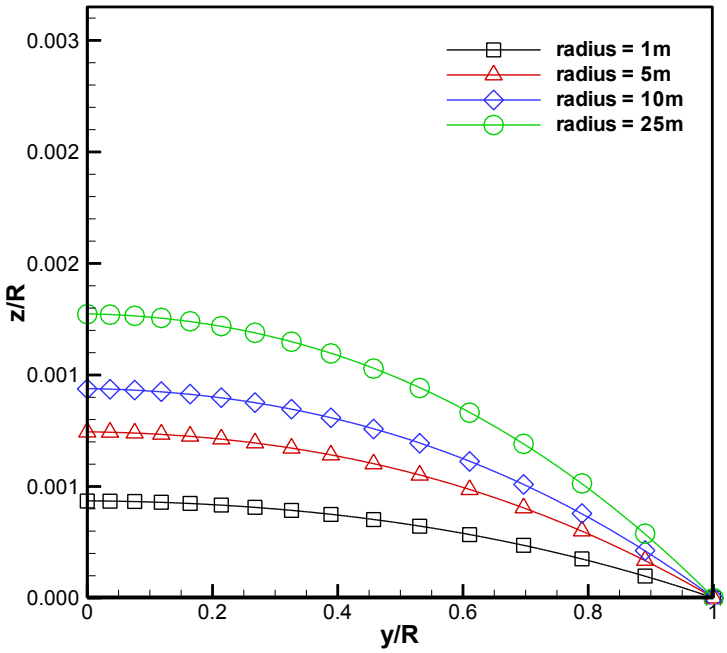

Figure D.3 - Non-dimensional displacement variation for the 8µm thickness membranes.

Annex E - FORTRAN® routine for geometric focus and light spot radius determination

Source File: Light

```
! ----------------------------------------------------------------------
! Light variables
  module LightVariables

  save

  integer ::       n,nx,np                          ! Nr of points
  real*8 ::        R,Rp                             ! Membrane Radius [m]
  real*8, allocatable :: x(:),y(:),theta(:),wf(:)! Function coordinates
  real*8 ::        wfmax                            ! Maximum value of abs(w) [m]
  real*8 ::        ytarget                 ! Variable to find Focal Distance [m]
  real*8 ::        F                       ! Aapproximate Focal Distance [m]
  real*8 ::        dx                      ! Point spacing [m]

end module LightVariables

! ----------------------------------------------------------------------
! Subroutine to calculate radius of solar light reflected at focal point
  subroutine Light()

  ! Modules
    use LightVariables

    implicit none

  ! Variables declaration
    integer ::   i
    real*8  ::   Pi

    Pi = 4.0*atan(1.0)

  ! Calculate intersection of light reflection with line y=ytarget
    wfmax = 0.0

    do i=1,n
    wf(i) = 1.0/tan(-Pi/2.0+2.0*theta(i))*(ytarget-y(i))+x(i)
    wfmax = max(wfmax,abs(wf(i)))
    end do

    return

end subroutine Light

! ----------------------------------------------------------------------
! Subroutine to minimize objective function using the slope of the function
  subroutine OptimizationSlope()

  ! Modules.
  use LightVariables

  ! Variables declaration
    implicit none

  ! Variable Declaration
    integer ::   j
    integer ::   turn
    real*8  ::   ytargetref
    real*8  ::   wfold,wfref
```

```
! Calculate approximate focal distance (adjust ytarget so that
max(abs(wf(i),i=1,nx)) is a minimum)
    turn    = 1
    ytarget = 200.0     !Parameter needs to be adjusted closed to expected
focal distance on each simulation
    wfold   = -1000.0
    wfref   = 0.0

  do j=1,10000
    ! Calculate intersection of light reflection with line y=ytarget
    call Light()
    ! Check divergence function.
    if(abs((wfmax-wfold)/wfold).LE.0.0001) exit
    call LinearFunctionZero(turn,1.0d3,ytarget,wfmax,ytargetref,wfref)

    wfold = wfmax
      if(j.GT.14) then
        ytargetref = ytarget+0.05*(ytargetref-ytarget)
      end if
    ytarget  = max(0.01,ytargetref)
  end do
  F = ytarget

  write(*,'(A)') ' -'
  write(*,'(A,I7,A,F20.4,A)') ' Iteration ',j-1,' - Approximate focal
distance: ',F,' m'

return
end subroutine OptimizationSlope
```

Source File: MainProgramme

```
! ------------------------------------------------------------------
! Program to calculate approximate focal distance
  program MainProgramme

  ! Modules.
  use LightVariables

  ! Variables declaration
  implicit none

  ! Variables declaration
  integer ::                    i,j          ! loop/index variables
  integer ::                    option       ! 1 = analysis; 2 = optimization
  character*2 ::                string        ! general string
  character*1 ::                answer

  ! Write heading to screen
    write(*,'(A)') ' '
    write(*,'(A)') ' Program to estimate focal distance  '
    write(*,'(A)') ' General Conceptual Design Problems of a Parabolic Space
Structure'
    write(*,'(A)') ' Master Thesis - University of Beira Interior'
    write(*,'(A)') ' Filipe C. Potes'
    write(*,'(A)') ' '

  ! Select between executing programme or end programme
  300 continue
  write(*,'(A)') ' '
  write(*,'(A)') ' Choose one option from the following...'
  write(*,'(A)') '  1 - Execute Programme'
  write(*,'(A)') '  2 - Cancel Programme'
  write(*,'(A)') ' '
```

```
  read(*,*) answer
  write(*,'(A)') ' '
  if(answer.EQ.'1') then
      option = 1
    else if(answer.EQ.'2') then
      write(*,'(A)') ' The End!'
        stop
       else
        goto 300
  end if

! Read input variables
  write(*,'(A)') ' Reading input data...'
  open(10,file = "input.txt")
  !read(10,'(A)') string
  !read(10,*) Rp
  read(10,'(A)') string
  read(10,*) np
  allocate(x(np),y(np))
  read(10,'(A)') string
  do i=1,np
    read(10,*) x(i),y(i)
  end do
  close(10)

! Rewrite input variables
  write(*,'(A)') ' Rewriting input data...'
  open(10,file = "input.txt")
  write(10,'(A)') 'Number of data points (np)'
  write(10,'(2I20)') np
  write(10,'(A)') 'Data points coordinates (x[m],y[m])'
  do i=1,np
    write(10,'(2E20.12)') x(i),y(i)
  end do
  close(10)

  ! Calculate theta
      dx = R/(n-1)
      n  = np
      allocate(theta(n),wf(n))
      R = x(n)
      ! Calculate angle of curve at nodes
      theta(1) = 0.0

      do i=2,n-1
         theta(i) = atan(0.5*((y(i+1)-y(i))/(x(i+1)-x(i))+(y(i)-y(i-1))/(x(i)-
x(i-1))))
      end do

      theta(n) = atan((y(n)-y(n-1))/(x(n)-x(n-1)))

  call OptimizationSlope()


  write(*,'(A,F20.4,A)') ' - Light radius at approximate focal distance:
',wfmax,' m'

  ! Write output data
    write(*,'(A)') ' Writing output data...'
    open(10,file="output.txt")
    write(10,'(A)') 'Focal distance (F[m])'
    write(10,'(2E20.6)') F
    write(10,'(A)') 'Radius of light reflected at focal plane (wfmax[m])'
    write(10,'(2E20.6)') wfmax
    write(10,'(A)') 'Data'
    write(10,'(A)') 'x, m   y, m   theta, rad     w, m'
       do i=1,n
    write(10,'(4E20.12)') x(i),y(i),theta(i),wf(i)
```

```
  end do
  close(10)

  ! Return to menu.
  write(*,'(A)') ' '
  goto 300

end program MainProgramme
```

Source File: Maths

```
! ----------------------------------------------------------------------
! Subroutine to obtain zero of a function by linear approximation
  subroutine LinearFunctionZero(turn,dx,x_old,y_old,x_new,y_new)

  ! Variables declaration
    implicit none

  ! Parameters
    integer, parameter ::     n = 2          ! number of points

  ! Input variables
    real*8, intent(in) ::     dx             ! increment in x
    real*8, intent(in) ::     x_old,y_old    ! initial values of x and y
    real*8, intent(in) ::     y_new          ! value of function required

  ! Input/output variables
    integer, intent(inout) ::  turn  ! 1=only one value exists, 2=only two
values exist

  ! Output varables
    real*8, intent(out) ::    x_new          ! required ordinate of function

  ! Local variables
  real*8, save ::      x(n),y(n)            ! x,y coordinates
  real*8 ::            slope                ! function slope approximation


  if(turn.EQ.1) then
      ! Only one value
        x(2) = x_old
        y(2) = y_old
       x_new = x(2)+dx
        turn  = 2
      else
        ! Define points
        x(1) = x(2)
        y(1) = y(2)
         x(2)= x_old
        y(2)= y_old

      ! Slope
      slope  = (y(2)-y(1))/(x(2)-x(1))

      ! Required value of x given value of y
      x_new         = x(1)+(y_new-y(1))/slope

  end if
return

end subroutine LinearFunctionZero
```